# CHEMICAL VAPOR DEPOSITION OF TRANSPARENT CONDUCTING OXIDE NANOSTRUCTURES ON VARIOUS SUBSTRATES FOR SOLAR CELL APPLICATIONS

_____

A Thesis

Presented to

The Faculty of the Department of Chemistry

Sam Houston State University

_____

In Partial Fulfillment

of the Requirements for the Degree of

Master of Science

_____

by

Hailey C. Stephen

August 2021

# CHEMICAL VAPOR DEPOSITION OF TRANSPARENT CONDUCTING OXIDE NANOSTRUCTURES ON VARIOUS SUBSTRATES FOR SOLAR CELL APPLICATIONS

by

Hailey C. Stephen

_____

APPROVED:

Tarek M. Trad, PhD
Committee Director

David E. Thompson, PhD
Committee Member

Darren L. Williams, PhD
Committee Member

John B. Pascarella, PhD
Dean, College of Science and Engineering Technology

## ABSTRACT

Stephen, Hailey C., *Chemical vapor deposition of transparent conducting oxide nanostructures on various substrates for solar cell applications*. Master of Science (Chemistry), August, 2021, Sam Houston State University, Huntsville, Texas.

Nanostructured wide band gap transparent conducting oxides are important in the optoelectronic industry. Chemical vapor deposition (CVD) is a simple and effective method for synthesizing high-quality nanostructures from bulk materials. Three areas were investigated during this research: the effects of a ZnO seed layer on ZnO nanowires grown on transparent substrates by CVD, the vapor-liquid-solid synthesis of nanostructures by CVD using graphite to reduce $Ga_2O_3$, and a preliminary study of dye-sensitized solar cell design and testing. The ZnO seed layer was shown to improve the vertical alignment and distribution of the synthesized ZnO nanowires on mica, fused quartz, and *c*-plane sapphire substrates. Scanning electron microscopy (SEM), energy dispersive X-ray spectroscopy (EDS), X-ray diffraction (XRD), and room temperature photoluminescence were used to characterize the ZnO nanostructures. Nanoparticles and nanowires were synthesized on Si(100) substrates with a 10-nm catalytic gold layer by varying the reaction conditions. However, these experiments were not always reproducible. The products were analyzed by SEM and EDS to determine the morphology and average chemical composition of the structures, but the small amount of deposition prohibited proper analysis of the crystal phase of the nanostructures by XRD and room temperature photoluminescence with the available instrumentation. Rudimentary dye-sensitized solar cells were fabricated using conductive glass, bulk $TiO_2$, N3 dye (cis-bis(isothiocyanato)bis(2,2′-bipyridyl-4,4′-dicarboxylato)ruthenium(II), and an $I^-/I_3^-$ redox couple electrolyte. These cells produced voltage measurements

comparable to literature values for similarly constructed cells, but the measured current was significantly lower than expected.

KEY WORDS: Zinc oxide, Gallium oxide, Nanostructures, Chemical vapor deposition, Dye-sensitized solar cell

## ACKNOWLEDGEMENTS

I am very grateful to my advisor, Dr. Tarek Trad, for his advice and supervision during the completion of my research. It has been a pleasure to work in Dr. Trad's lab during my time at Sam Houston State University, and I would like to thank all my fellow group members for their encouragement. I would especially like to acknowledge Parker Blount, who was very instrumental in the completion of this research.

I would like to thank Dr. David Thompson for his help with instrumentation and his constant efforts to shape all his students into better scientists. I am also thankful to Dr. Darren Williams who has been a great teacher and a wonderful source of knowledge and wisdom. I greatly appreciate the efforts of Dr. Dustin Gross, Dr. Donovan Haines, Rachell Haines, and all the faculty and staff of the chemistry department to keep me on track and moving forward in this journey. I am extremely grateful for the skills I have learned, and I will certainly reflect on this time in my life for many years to come.

Finally, I would like to express my gratitude to all my family and friends who have continuously supported me in this challenging endeavor.

## TABLE OF CONTENTS

**Page**

## LIST OF TABLES

**Table** **Page**

## LIST OF FIGURES

**Figure** **Page**

# CHAPTER I

# Introduction

## Applications and Significance

Although there has been a movement towards the use of clean energy sources, fossil fuels still supply most of the world's energy. Research of techniques to efficiently tap into solar, wind, geothermal, and hydropower resources is an integral step in the diversification of energy production. The unique properties of metal oxide nanomaterials compared to bulk materials has been revolutionary in the field of material science, especially for solar cell applications. They have been used to engineer photoelectric devices known as dye-sensitized solar cells that have been hypothesized to have the capability to be more efficient, more cost effective, and more environmentally friendly compared to current solar energy-harvesting options. It is also possible for them to be transparent, which presents a wide range of possibilities for installation.

## Dye-Sensitized Solar Cells

The first dye-sensitized solar cell (DSSC), also known as a Grätzel cell, was reported by O'Regan and Grätzel in 1991.[1] This type of cell consists of five component (Figure 1): a conductive working electrode (a), nanomaterial (b), a photosensitizing agent (c), an electrolyte solution (d), and a conductive counter electrode(e).

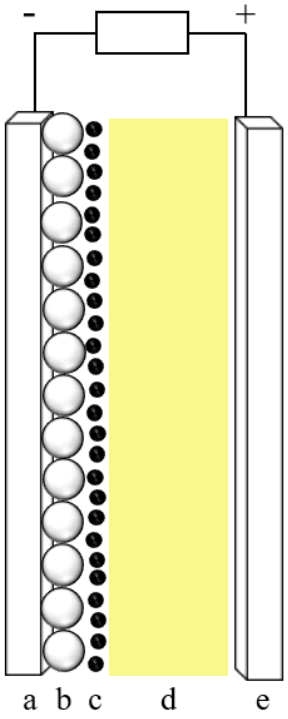


*Figure 1.* Components of a dye-sensitized solar cell.

The original design included the following for the five components in order a - e: conductive glass, high surface area $TiO_2$ film, ruthenium-based dye, $I^-/I_3^-$ electrolyte solution, and conductive glass, respectively. This design achieved a 7.1-7.9% power conversion efficiency (PCE) when the cell was exposed to simulated sunlight.[1]

PCE (η) of a DSSC is the percentage of the light energy ($P_{input}$) that is converted to electrical energy by the cell ($P_{max}$).

$$\eta = \frac{P_{max}}{P_{input}} \text{ x } 100\% \quad (1)$$

The power input is based on the quantity of light energy directed onto the cell. The power output is dependent on the following properties typically reported for a cell:

the short-circuit current ($I_{SC}$), the open-circuit voltage ($V_{OC}$), and the fill factor (FF). Therefore, the equation for calculating PCE of a DSSC can also be written as shown in Equation 2.

$$\eta = \frac{I_{SC}V_{OC}FF}{P_{input}} \text{ x } 100\% \quad (2)$$

The short-circuit current is the maximum amount of current that can flow through the cell. It is measured when the voltage is 0 by eliminating resistance in the circuit. Open-circuit voltage is the maximum voltage achieved by the cell where there is no current flowing through the cell. Since power is calculated using Equation 3, the power of the cell at the points where the $I_{SC}$ and the $V_{OC}$ occur is 0 watts.

$$P = I \text{ x } V \quad (3)$$

The fill factor (Equation 4) of a cell is the ratio of the maximum power ($P_{max}$) generated by the cell to the product of the $I_{SC}$ and the $V_{OC}$ values.

$$FF = \frac{P_{max}}{I_{SC} \, x \, V_{OC}} = \frac{I_M \, x \, V_M}{I_{SC} \, x \, V_{OC}} \quad (4)$$

In Figure 2, voltage (x-axis) is plotted against current (y-axis) to produce a typical I-V curve. Area A is the largest rectangle that will fit inside the I-V curve, and area B is the area encompassed between the axes and the point with the coordinate ($V_{OC}$, $I_{SC}$). The fill factor describes the ratio between these two areas $\left(\frac{area\ A}{area\ B}\right)$. Area A will be larger for cells with higher fill factors. Because the power is 0 W when I = $I_{SC}$ or V = $V_{OC}$, area A must be smaller than area B.

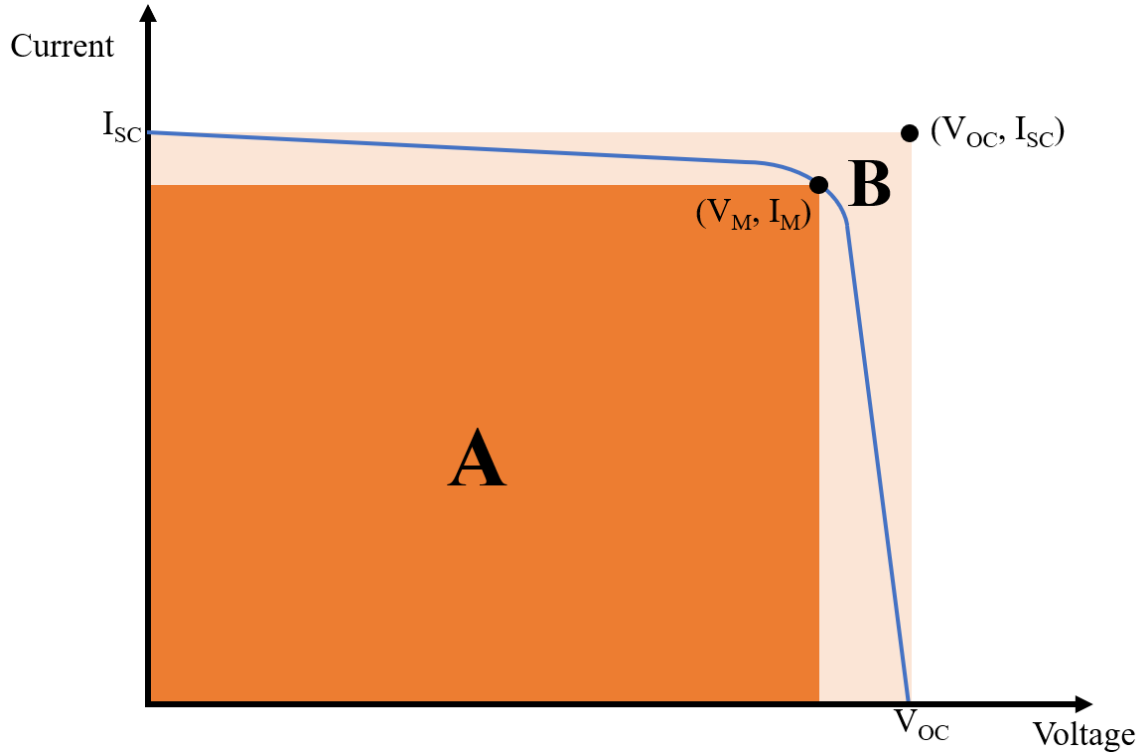


*Figure 2*. Typical I-V curve with a fill factor visual representation.

DSSCs are photoelectric devices in which the movement of electrons is initiated by exciting photoactive dye molecules with photons to generate excitons, or electron-hole pairs. The ability of the semi-conductor on the working electrode to bind the electrons from these electron-hole pairs is a critical property. The electrons released from the dye molecules in their excited state are injected into the nanomaterial to which the dye is adsorbed and carried through the working electrode. The electrolyte solution then reduces the dye molecules to their original state, and the counter electrode reduces the

electrolyte solution to complete the circuit. Figure 3 illustrates the processes that take place in the DSSC to generate electrical energy when exposed to sunlight.

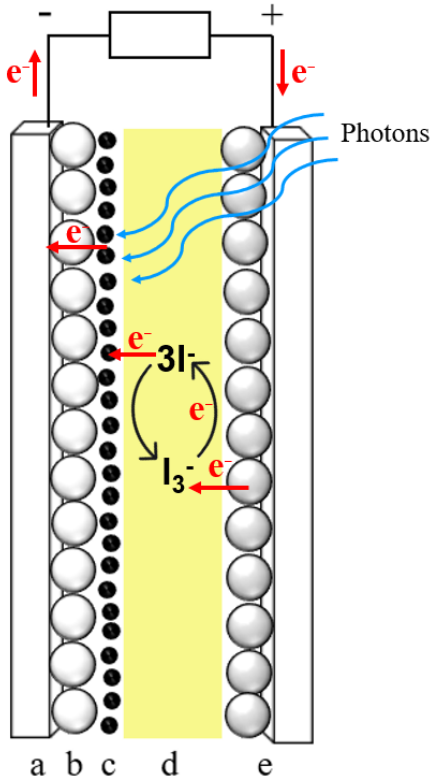


*Figure 3.* Illustration of the electron flow through a dye-sensitized solar cell.

The sensitizing agent is adsorbed to the metal oxide layer on the photoanode for efficient transfer of the injected electrons. There have been a variety of sensitizers incorporated into DSSCs as the photoactive portion of the cell. The most notable sensitizer developments include ruthenium polypyridyl dyes, metal-free dyes, porphyrin dyes, quantum dot sensitizers, and perovskite sensitizers. The most efficient cells for each of the sensitizers have been based on $TiO_2$.

Ruthenium polypyridyl dyes consist of a ruthenium metal center coordinated with various ligands. These were among the first sensitizers used in DSSCs, including the original design. This design was able to reach a 7.1-7.9% PCE when exposed to

simulated sunlight.[1] Progress was made to accomplish up to a PCE of 11.5% by enhancing the heteroleptic ruthenium complex (multiple types of ligands) with a hexylthio-terminal chain to provide additional electron density.[2] Metal-free dyes are derived from several groups of organic molecules and are more cost-effective, more environmentally friendly, and can produce results similar to ruthenium-containing complexes. For example, organic indoline dyes have a higher molar coefficient as opposed to the ruthenium complex used in the first DSSC, and modifications with rhodamine rings allowed for a red-shift in absorption spectra to give an overall PCE of 8%.[3] Further increase of the molar coefficient and absorption spectra in a sensitizer based on triazatruxene achieved a PCE of 13.6% in 2019.[4]

Porphyrins are large ring systems that often contribute to harvesting energy from sunlight in photosynthesis. Porphyrin dyes generally have high molar extinction coefficients, structural diversity, and reasonable stability.[5] These qualities are all necessary in a DSSC. In 2011, a porphyrin-sensitized DSSC achieved a maximum PCE of 12.3% when co-sensitized with an organic dye and paired with a Co(II/III) electrolyte.[6] At this time, zinc-porphyrin dyes have been the sensitizer in all of the record porphyrin-sensitized solar cells. Computational studies have resulted in structure optimization to increase light-harvesting capabilities.[5, 7] Incorporating these findings, a porphyrin dye exhibited a 13% PCE in 2014.[7]

Quantum dots and perovskites are popular inorganic sensitizers. Co-sensitization with quantum dots (CdS/CdSe, CdTe/CdSe) has been shown to decrease exciton recombination exhibiting a 6.76% PCE.[8] The material, synthesis method, and interfacing techniques are key factors for high efficiency.[9] In 2017, a Zn-Cu-In-Se solid state QDSC

achieved a 12.34% PCE.[10] Perovskites are a group of materials with the crystal structure of $CaTiO_3$, such as crystalline halides. This sensitizing agent has quickly advanced to the forefront of solar technology research. As of 2016, perovskite sensitizers reached a peak PCE of 19.1% in an inorganic-organic hybrid cell.[11] Perovskites have also been incorporated into perovskite/silicon tandem cells with 25.2% PCE.[12]

There are fewer common electrolytes used in DSSCs. Many of the record PCEs for DSSCs have been achieved using a $I_3^-/I^-$ electrolyte. It is the most POPULAR electrolyte because of its good solubility, low light absorbance, low cost, stability, low recombination rate, and high dye regeneration rate.[13] Often, the electrolyte is within an organic solvent, but a liquid electrolyte can be a disadvantage in the current DSSC design because of degradation, leakage, and evaporation possibilities. Quasi-solid and solid electrolytes are alternatives that have been explored. Although, there is generally a decrease in PCE values compared to those achieved with a liquid electrolyte. This may be caused by a decrease in electrolyte molecules interacting with the metal oxide layer.[14-16] However, recent developments have allowed a 9.21% PCE to be obtained using a quasi-solid state electrolyte.[17] Using copper(II/I) hole transport materials to improve conductivity, a solid-state DSSC achieved a PCE of 11%.[18]

Counter electrodes must have superior conduction, stability, and catalytic properties to effectively mediate the electrolyte redox couple. Au, Ag, and Pt are often used for this DSSC component, especially Pt. P-type metal oxide layers may also be an option for counter electrodes, which would create the potential for an oxide-based DSSC.[19] $Cu_2O$ and fluorine-doped tin oxide (FTO) are commonly used in these types of

cells. Doping ZnO with Sb, N, and Cu have been shown to produce p-type conduction, which could be used as a counter electrode.[20-22]

As opposed to thin films, one dimensional nanostructures are hypothesized to increase efficiency of electron transfer from the dye to the working electrode, particularly ordered nanowire arrays.[23] Other transparent conducting oxides (TCO) such as gallium oxide, zinc oxide, tin oxide, and composites of these materials have been used to modify the layer.[24] ZnO has been extensively researched as an alternative because of its abundance, electronic properties similar to $TiO_2$, and ample facile growth techniques.

**ZnO Overview**

Along with $TiO_2$, ZnO has been used commercially in paint, cosmetic, and sunscreen products. ZnO is a TCO with similar electronic properties compared to $TiO_2$. It has a large band gap of 3.37 eV and it intrinsically exhibits n-type semiconduction. Like $TiO_2$, ZnO has been shown to exhibit p-type semiconduction with the introduction of dopants, such as antimony or copper, into the crystal lattice. It has a large exciton binding energy of 60 meV. An exciton is an electron-hole pair formed when a semiconductor absorbs a photon of higher energy than its band gap and an electron moves from the conduction band into the valence band. The exciton binding energy of a semiconductive material can be calculated based on the effective masses of electrons and holes for that specific material, and higher values correspond to greater stabilization of excitons. Crystalline ZnO exhibits either hexagonal wurtzite structure (Figure 4a) or cubic (zinc blende) structure (Figure 4b).

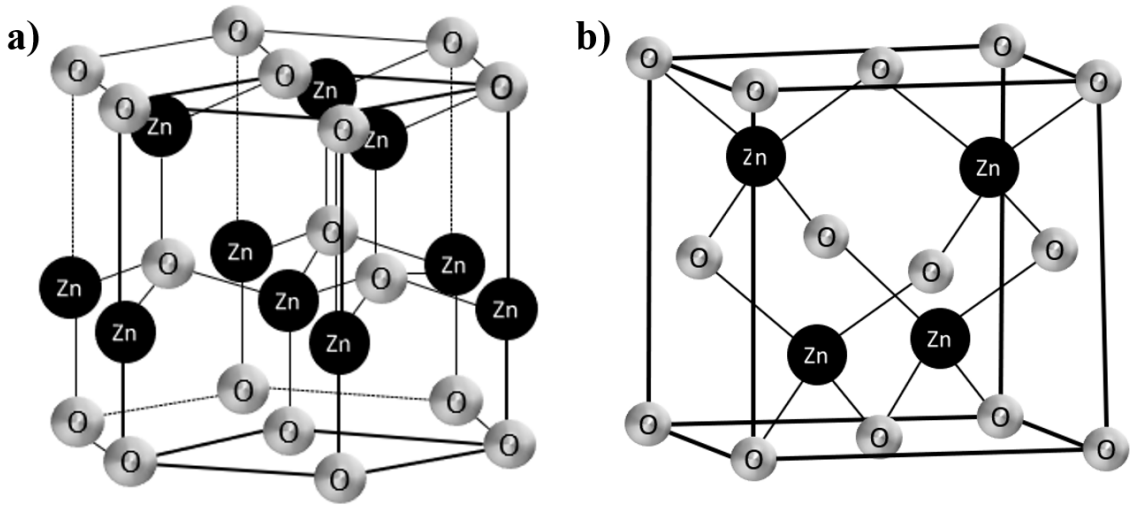


*Figure 4.* Crystal structures of ZnO.

**ZnO Morphologies and Synthesis Methods**

ZnO has reportedly been synthesized in many different morphologies by a variety of synthesis methods, while $TiO_2$ morphologies and synthesis methods are more limited.

ZnO nanowires, nanosheets, nanoflowers, nanopyramids, and other morphologies have been reported in the literature. Ordered nanowire arrays are typically the morphology used in DSSCs as they have a surface area to volume ratio and a more direct path for electrons from the dye to the working electrode. Chemical synthesis methods for ZnO nanostructures include sol-gel, hydrothermal, electrodeposition, and sputtering. Nanostructures produced by these methods are typically of lower crystal quality caused by a higher probability of incorporating contaminants in solution growth. Physical synthesis methods include chemical vapor deposition (CVD), atomic layer deposition (ALD), thermal evaporation, molecular beam epitaxy (MBE), and pulsed laser deposition (PLD). Higher crystal quality, higher growth rates, more precise control over reaction conditions, and minimal solvent use generally accompany physical synthesis methods.

However, since higher temperatures may be required, some physical methods may not be suitable for all substrates.

**ZnO Challenges in Dye-Sensitized Solar Cells**

While facile synthesis methods have been developed for ZnO nanowire arrays, many of the dyes used in $TiO_2$-based DSSCs are hypothesized to form complexes with $Zn^{2+}$ on the surface of the nanostructures. This causes a decrease in the flow of electrons directed through the metal oxide to the working electrode and overall lower PCE values. Further research into a compatible dye component for ZnO-based DSSCs will likely be key in improving PCE values for these devices; however, this is not currently an objective of our lab.

**Gallium Oxide**

Compared to other TCOs, relatively little research has been conducted on $Ga_2O_3$. It has piqued the interest of many researchers with its ultra-wide band gap of 4.9 eV and robust chemical and thermal stability. Gallium oxide is an intrinsic insulator, but it has been shown to exhibit n-type semiconduction when the band gap of the material is reduced by the presence of dopants or oxygen vacancies in the crystal lattice. $Ga_2O_3$ has been reported to exist as five different phases including: corundum (α), monoclinic (β), spinel (γ), bixbyite (δ), and orthorhombic (ε). However, the δ phase is considered by some researchers to be a deformed ε phase. Potential applications of $Ga_2O_3$ include use in transistors, gas sensors, photodetectors, and solar cells. However, a significant amount of the research in this area has been devoted to the former three applications.

Chemical vapor deposition (CVD), atomic layer deposition (ALD), thermal evaporation, molecular beam epitaxy (MBE), sputtering, sol-gel, and hydrothermal

methods have been reported for the synthesis of various $Ga_2O_3$ nanostructures. Hydrothermal methods have been used to synthesize β-$Ga_2O_3$ nanorod arrays for photodetection.[25] CVD has been used to synthesize $Ga_2O_3$ on substrates with catalysts such as gold,[26] on substrates coated with a $Ga_2O_3$ seed layer,[27] and on substrates with no catalytic layer.[28] The morphologies reported using these methods include nanowires, nanorods, and nanosheets.

**Goals of This Research**

The first goal of this research was to study the effect of ZnO nanostructure growth on a ZnO seed layer on various transparent substrates. The ability to reliably produce ordered nanowire arrays on transparent substrates is important for the construction of transparent solar cells. Knowledge from work done with ZnO seed layers on Si(100) substrates previously by the lab was used as a starting point. Secondly, synthesis of $Ga_2O_3$ by a CVD method similar to the process used for depositing ZnO was investigated. Preliminary studies were conducted to begin developing a method for synthesizing $Ga_2O_3$ by carbothermal reduction CVD. A rudimentary dye-sensitized solar cell was fabricated and tested to gain understanding of the fundamental procedures of building and characterizing solar cells.

# CHAPTER II

## Effects of a ZnO Seed Layer on the Growth of ZnO Nanowires on Various Transparent Substrates by Chemical Vapor Deposition

### Introduction

Chemical vapor deposition has several benefits compared to other nanostructure synthesis methods. Important features include high growth rates, high product purity, minimal solvent use, and facile control of experimental parameters such as temperature, pressure, and gas flow. Carbothermal reduction of bulk ZnO at high temperature enables the vaporization of zinc. Figure 5 depicts the proposed mechanism for chemical vapor deposition of ZnO nanowires using a solid ZnO and carbon precursor.

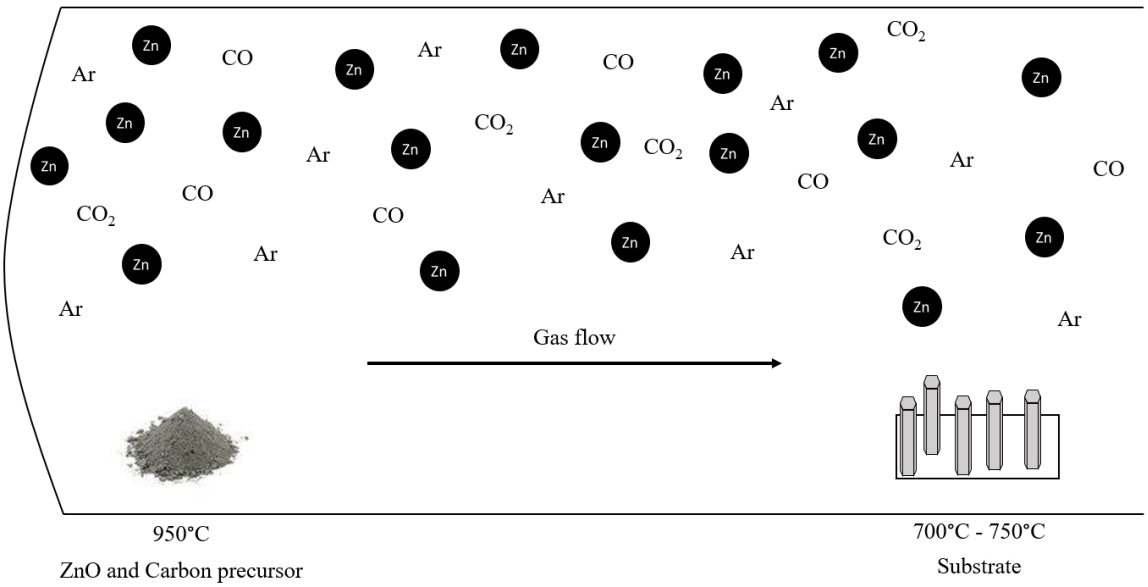


*Figure 5.* Illustration of the proposed CVD mechanism.

Carbon in the solid precursor reduces zinc oxide to form zinc vapor, and carbon is oxidized to carbon monoxide. Carbon monoxide may reduce ZnO to form zinc vapor and carbon dioxide. Zinc vapor either reacts with oxygen in the reaction chamber to deposit

as solid ZnO hexagonal nanocolumns on the substrate, or it deposits as metallic Zn islands.

$$ZnO_{(s)} + C_{(s)} \rightarrow Zn_{(g)} + CO_{(g)} \quad (5)$$

$$ZnO_{(s)} + CO_{(g)} \rightarrow Zn_{(g)} + CO_{2(g)} \quad (6)$$

$$2Zn_{(g)} + O_{2(g)} \rightarrow 2ZnO_{(s)} \quad (7)$$

The deposition of ZnO on a substrate without the presence of a catalyst occurs by a vapor-solid mechanism, which is highly dependent on the amount of crystal mismatching between the surface of the substrate and the lattice pattern of the ZnO nanostructures.

Previously, a temperature profile of the tube furnace was determined from 220-730°C in 0.5 cm increments when the center of the tube furnace was 950°C. Our lab has also studied the growth of vertical nanocolumns on Si(100) substrates catalyzed by Au or self-catalyzation by depositing a ZnO seed layer onto the substrate surface. The hexagonal nanocolumns with diameters ranging from 80-150 nm are shown in the SEM image in Figure 6a. The average atomic composition of the sample was 44.6% Zn and 56.4% O. From analysis with powder x-ray diffraction, six peaks were indexed to the wurtzite form of ZnO (Figure 6b). Room temperature photoluminescence data showed a trend between the decrease of intensity of the broadband emission peak around 500 nm with the increase of reaction time (Figure 6c). Nanocolumn diameter was shown to have a positive linear correlation with reaction (Figure 6d).

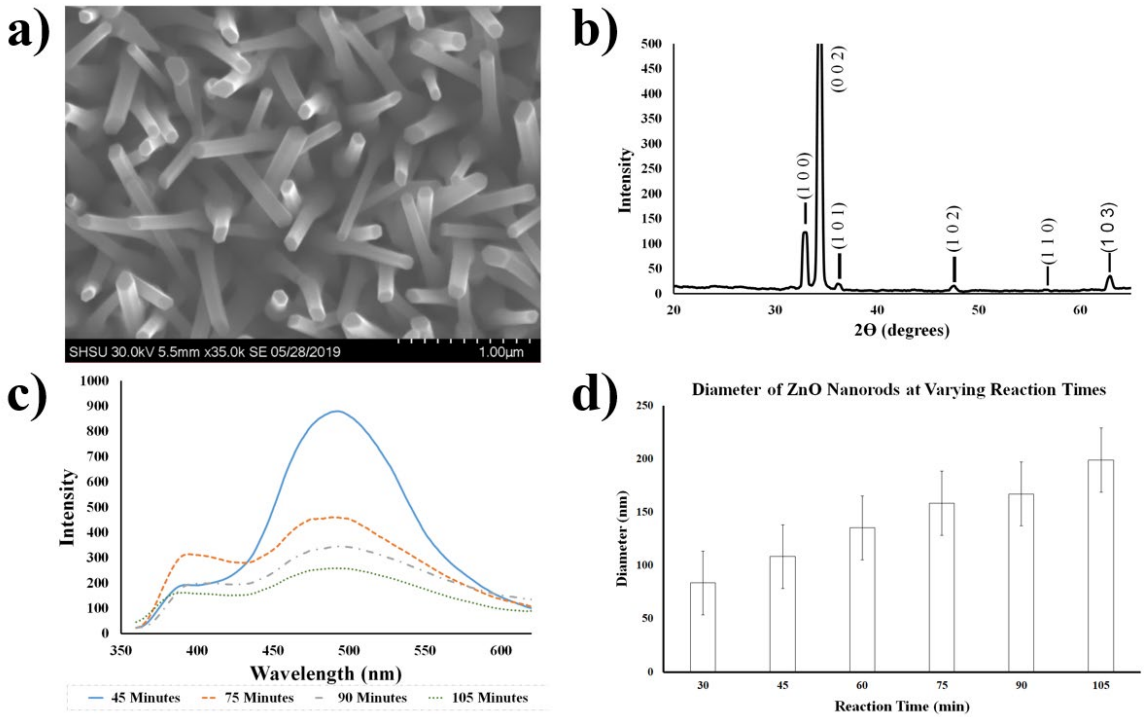


*Figure 6.* Characterization of previous work with ZnO.

The effects of growing ZnO nanowires on a ZnO seed layer compared to growth on bare transparent substrates are reported in this chapter. The substrates were characterized by scanning electron microscopy (SEM), energy dispersive x-ray spectroscopy (EDS), x-ray diffraction (XRD), and room temperature photoluminescence (PL).

**Materials and Methods**

All materials and reagents were purchased from commercial sources and used without further modification. Chemical vapor deposition was achieved using a tube furnace (OTF-1200), a gas supply system (GSL-3Z), and a vacuum pump (PV-HVS2) from MTI Corporation, Inc.

### *Cleaning of Substrates*

To remove residual organic material, all substrates were cleaned by 10 minutes of sonication in ethanol (200 Proof, Sigma Aldrich) followed by sonicating for 10 minutes in acetone (99.5%, VWR Chemicals). The substrates were then dried under flowing $N_2(g)$.

### *ZnO Seed Layer Application*

A 5.5 mM solution of zinc acetate dihydrate (≥98%, Sigma Aldrich) was made in diethyl ether. In a quartz boat on a low-heat (~50°C) hot plate, the tops of the substrates were covered with this solution. The substrates were annealed at 150°C for 45 minutes once the solvent had evaporated. The solution was applied to the substrates a second time in the same fashion followed by annealing for 1 hour.

### *Chemical Vapor Deposition of ZnO*

Equimolar amounts of bulk ZnO (99.999%, Goodfellow) and graphite (<20 μm, synthetic, Sigma Aldrich) were homogenized to form a uniformly grey powder using a mortar and pestle. This precursor was transferred to the closed end of the reaction tube depicted in Figure 7. For experiments with mica substrates (Electron Microscopy Sciences), the fused quartz reaction tube used was 25 cm in length and had an interior diameter of 1.2 cm. The fused quartz reaction tube used for experiments with fused quartz (FQ-S-001, AdValue Technology) and *c*-plane sapphire (AdValue Technology) substrates was 29.5 cm in length with an interior diameter of 1.5 cm. The substrate was placed just inside the open end of the reaction tube, shown in Figure 7, with about 1.6 cm

*Figure 7.* CVD fused quartz reaction tube with substrate and precursor.

from the opening to the nearest edge of the substrate. The reaction tube was then transferred to the furnace tube, shown in Figure 8. The temperature profile was previously taken of the furnace tube when the reaction temperature was set to 950°C. A ceramic thermometer was held at each 0.5 cm interval (relative to the end of the insulation on the right side of the furnace) for one minute used to record the temperatures in the right side of the furnace tube when the heated portion was stabilized at 950°C. The process was completed three times and the temperatures were averaged for each location in the furnace to determine the temperature profile of the furnace tube heated to 950°C. The middle of the substrate was placed 3.5 cm to the left of the end of the insulation as shown in Figure 8. The reaction conditions, shown in Table 1, were the same for all experiments with ZnO.

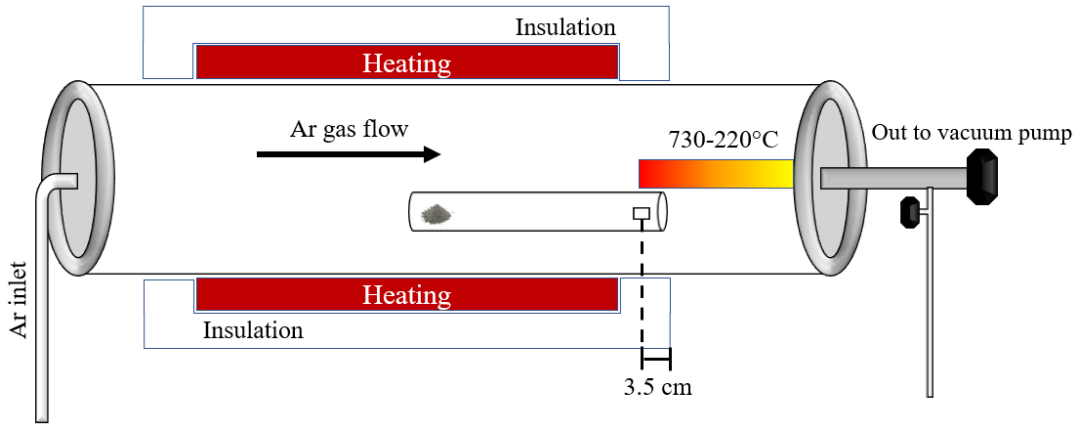


*Figure 8.* Tube furnace used for chemical vapor deposition.

*Table 1.* Reaction conditions used for synthesis of ZnO nanostructures by CVD.

| Experimental Parameters | Conditions |
|---|---|
| Pressure | 3.4 hPa (2.55 Torr) |
| Gas flow | 80 $cm^3$/min Ar(g) |
| Precursor temperature | 950°C |
| Heating rate | 10°C/min |
| Substrate temperature | 730°C |
| Reaction time | 60 minutes |

### *Characterization of ZnO Nanostructures*

Synthesized nanostructures were imaged by scanning electron microscopy (Hitachi SU3500) to determine the size, shape, and distribution of the nanostructures. Energy dispersive X-ray spectroscopy (EDS) was coupled with SEM to confirm the ratios of zinc to oxygen atoms in the scanned nanostructures. The crystal phase of the zinc oxide nanostructures was established by characterization using powder x-ray diffraction spectroscopy (powder XRD, Rigaku MiniFlex600 powder x-ray diffractometer). Room temperature photoluminescence (Hitachi F-4500 fluorescence spectrophotometer) was used to indicate the relative amount of oxygen vacancies and defects present in the nanostructures. A stage adapted for solid samples was used to mount the substrates in the path of the 325 nm excitation beam to collect emission readings from 350 nm to 600 nm.

## Results and Discussion

ZnO nanostructures were successfully synthesized on various transparent substrates: fused quartz, *c*-plane sapphire, and mica. These experiments were shown to be reproducible using the methods described above.

***Morphology***

Scanning electron microscopy (SEM) is one of the most common tools used to image nanostructures grown on substrates. Properties such as the shape, height, and diameter of the nanostructures can be visualized using this powerful technique. By scanning with a focused electron beam, resolutions of 2 nm can be achieved in some cases. Samples must be conductive, semi-conductive, or coated with a conductive layer to allow for interaction with the electron beam.

Generally, an SEM is equipped with a secondary electron detector and a back-scattered electron detector. Secondary electrons are produced by inelastic scattering of the electrons from the primary beam, and they have lower energy due to energy lost in exciting an electron in the sample. Backscattered electrons are involved in elastic scattering to rebound from the sample to a detector directly above the sample. Secondary electrons produce an image that encompasses more fine details, while backscattered electrons provide more contrast in the image. Therefore, the SEM images in this section were produced using secondary electrons.

As shown in Figure 9, it was demonstrated that depositing a ZnO seed layer on the surface of the substrates prior to the growth of ZnO nanocolumns by vapor phase transport generally improved the vertical alignment of the nanocolumns for the three types of transparent substrates investigated. This suggests that the seed layer can reduce the effects of crystal mismatching between the substrate and the ZnO nanostructures to allow growth of well-aligned nanocolumns. Table 2 contains the average heights and diameters of the ZnO nanowires grown on each of the different substrates.

*Table 2***.** Average heights and diameters of ZnO nanowires synthesized on various substrates by CVD.

| **Substrate** | **Average height of nanowires** | **Average diameter of nanowires** |
|---|---|---|
| Bare mica | 700 nm | 40 nm |
| Mica with ZnO seed layer | - | 180 nm |
| Bare c-plane sapphire | - | - |
| *c*-plane sapphire with ZnO seed layer | 570 nm | 90 nm |
| Bare fused quartz | 2.75 µm | - |
| Fused quartz with ZnO seed layer | 570 nm | 200 nm |

*Note:* Missing values were unable to be obtained using the available data (Figure 9).

Clear morphological changes are observed in the ZnO nanostructures on all the substrates with the addition of a ZnO seed layer. However, it appeared that the morphology continued to be slightly affected by the identity of the substrate despite the presence of a seed layer. Nanowires with an average diameter of approximately 40 nm and an average height of 700 nm were grown on the bare mica substrate. The atomic percentage of Zn was 72.5% compared to 27.5% oxygen. The substrate with a ZnO seed layer had a ratio of Zn to O that was close to 1:1 which is what is expected based on the

chemical formula. The diameter of these structures increased to 180 nm, but the height could not be estimated using this image.

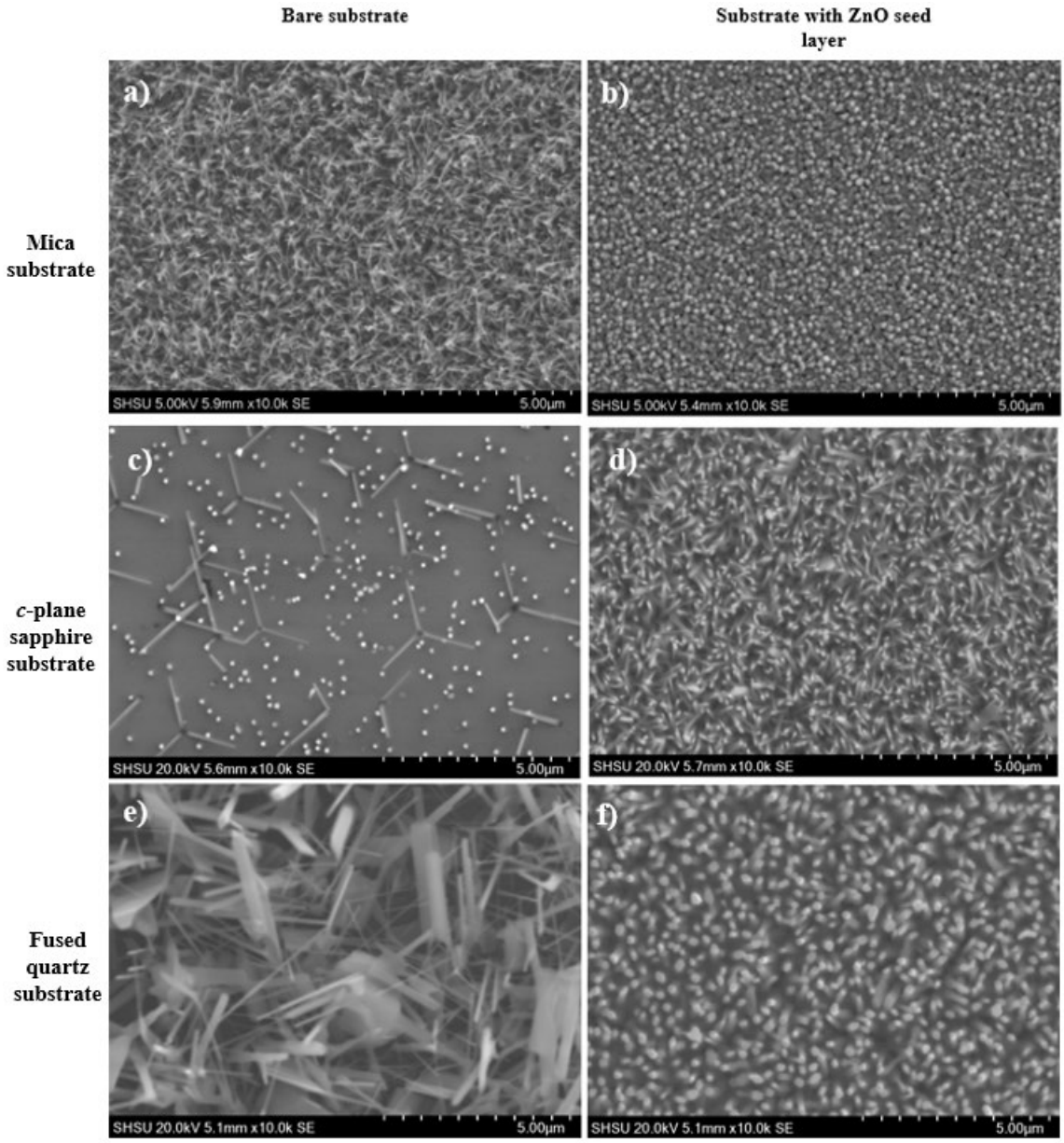


*Figure 9.* SEM images of synthesized ZnO nanostructures. a) bare mica substrate, b) mica substrate with ZnO seed layer, c) bare c-plane sapphire substrate, d) c-plane sapphire substrate with ZnO seed layer, e) bare fused quartz substrate, f) fused quartz substrate with ZnO seed layer.

Sparse deposition was observed on the bare sapphire substrate; however, the EDS analysis showed the atomic percentage of Zn to be 73% to 27% O, which is similar to

what was seen on the bare mica substrate. The density of nanocolumns deposited on the substrate with a ZnO seed layer increased noticeably, and the ratio of Zn to O was shifted towards 1:1 as seen with the mica experiments. The average height of the nanocolumns was 570 nm, and the average diameter was 90 nm.

Nanowires and nanosheets were formed on the bare fused quartz substrate with an average height of 2.75 um, a 77% atomic percentage of Zn, and a 23% atomic percentage of O. With the ZnO seed layer, the atomic percentage ratio became near 1:1 and the vertical-alignment and uniformity of the deposition improved. The nanocolumns on the fused quartz with the ZnO seed layer were estimated to have an average height of 570 nm and an average diameter of 200 nm.

***Atomic Composition***

Often, EDS is combined with SEM analysis to provide information about the chemical makeup of the sample, typically reported as mass percentages and subsequently converted to atomic percentages. When the sample is bombarded with electrons, inner shell electrons are ejected from atoms in the sample. The movement of an outer shell electron into the inner shell to replace the ejected electron causes the release of x-ray radiation with energy characteristic of the element. Points and areas of the sample can be analyzed, and mass percentages of each element are reported for individual points or areas as well as the average for the sample. The average atomic percentages are reported in Table 3 for the ZnO nanostructures grown on various transparent substrates.

*Table 3.* Atomic percentages of Zn and O from EDS analysis of ZnO nanostructures on various substrates.

| Substrate | Zn atomic% | O atomic% |
|---|---|---|
| Bare mica (a) | 72.5 | 27.5 |
| Mica with ZnO seed layer (b) | 44 | 56 |
| Bare c-plane sapphire (c) | 73 | 27 |
| c-plane sapphire with ZnO seed layer (d) | 58 | 42 |
| Bare fused quartz (e) | 77 | 22 |
| Fused quartz with ZnO seed layer (f) | 53 | 47 |

It can be observed from the atomic percentages of zinc and oxygen in Table 3 that substrates coated with a ZnO seed layer (b, d, and f) have a chemical composition closer to the expected 1:1 ratio of zinc to oxygen than those grown without the seed layer (a, c, and e). In comparison, the zinc and oxygen ratios were consistently about 1:3 on the bare substrates.

***Crystal Phase***

Powder x-ray diffraction (XRD) is commonly used to determine the crystal phase of bulk crystalline materials. X-ray radiation is aimed from the source onto the sample. The x-rays are scattered by the atoms in the crystal lattice onto a detector at an angle referred to as $2\Theta$ (Figure 10).[29] The detector moves relative to the sample to measure the signal at various $2\Theta$ values.

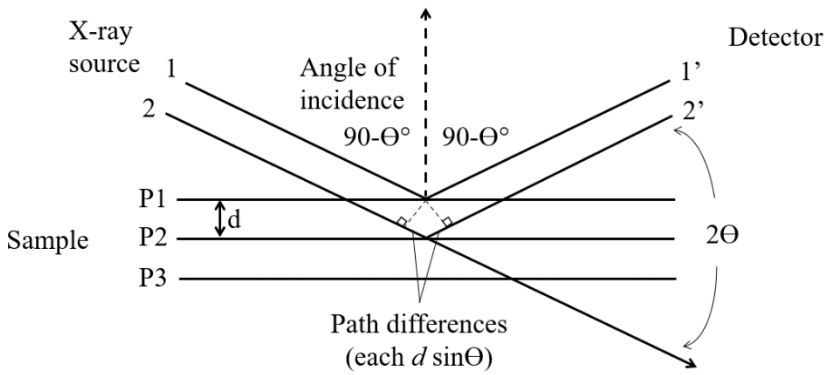


*Figure 10.* Diagram of XRD analysis.

Information about the spacing and arrangement of the atoms in the lattice can be determined using the information from the scattered electrons and Bragg's law (Equation 8) where $n$ is an integer, $\lambda$ is the x-ray wavelength, $d$ is the spacing in the crystal layers, and $\Theta$ is the angle at which the radiation hits the sample.

$$n\lambda = 2d\sin\Theta \tag{8}$$

The results are presented in a diffractogram where the intensity of the signal is plotted against the value of $2\Theta$ where the reflections of different planes in each crystal structure have peaks at characteristic $2\Theta$ values. XRD can also be used to analyze the preferred growth orientation of a material by using the intensities of the peaks as an approximation. An improvised stage, shown in Figure 11, was constructed to

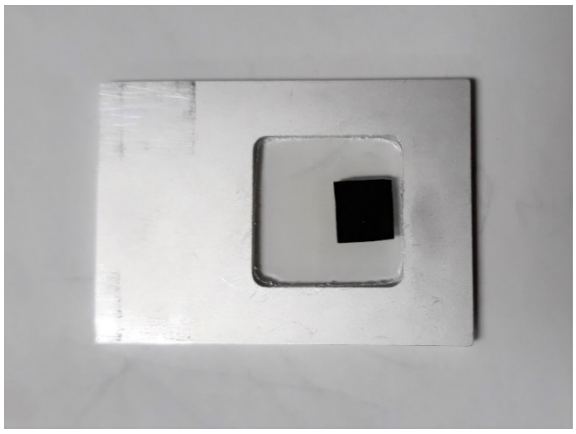

*Figure 11.* XRD stage adapted for substrate analysis.

accommodate the analysis of nanostructures grown on a substrate using powder XRD. Diffractograms, shown in Figure 12, were collected from $2\Theta$ values of 20-80° with a step size of 0.05° at a speed of 10°/min. Peaks corresponding to the reflections from the (002) and (004) planes of the wurtzite structure of ZnO (COD 1101258) were present in the diffractogram of the ZnO nanowires grown on a bare mica substrate (Figure 12a). Growth in the (002) direction appeared to be preferential based on peak intensity. When the seed layer was applied on mica before synthesis of ZnO nanowires by CVD (Figure 12b), the synthesized ZnO nanowires did not exhibit a significant reflection from the (004) plane of wurtzite ZnO, but the (002) reflection was maintained. The unidentified peaks present in these two diffractograms correspond to the crystal structure of the mica substrate. The (100), (002), (101), (102), (103), and (004) planes were present in the ZnO nanostructures grown on the bare *c*-plane sapphire substrate (Figure 12c), with the (002) plane being the most prominent. The addition of the ZnO seed layer decreased the number of peaks in the diffractogram (Figure 12d) showing only the reflections from the (002), (101), and (004) planes remain in this sample. The intensities of the peaks produced by the ZnO nanostructures grown on bare fused quartz (Figure 10e) were significantly decreased compared to the other samples. Reflections from the (100), (002), and (101) planes were slightly larger than the background noise from the substrate. Unlike the other samples that had a more prominent (002) peak, the peak from the (101) plane was slightly more intense than the (002) peak. ZnO nanowires grown on top of a ZnO seed layer deposited on a fused quartz substrate exhibited defined peaks indicating the presence of the (002) and (004) planes of wurtzite ZnO (Figure 12f). Overall, growth in the (002) direction appears to be preferential for the ZnO nanostructures grown on the

three substrates with or without a ZnO seed layer. The diffractograms of bare substrates before growth can be found in the Appendix.

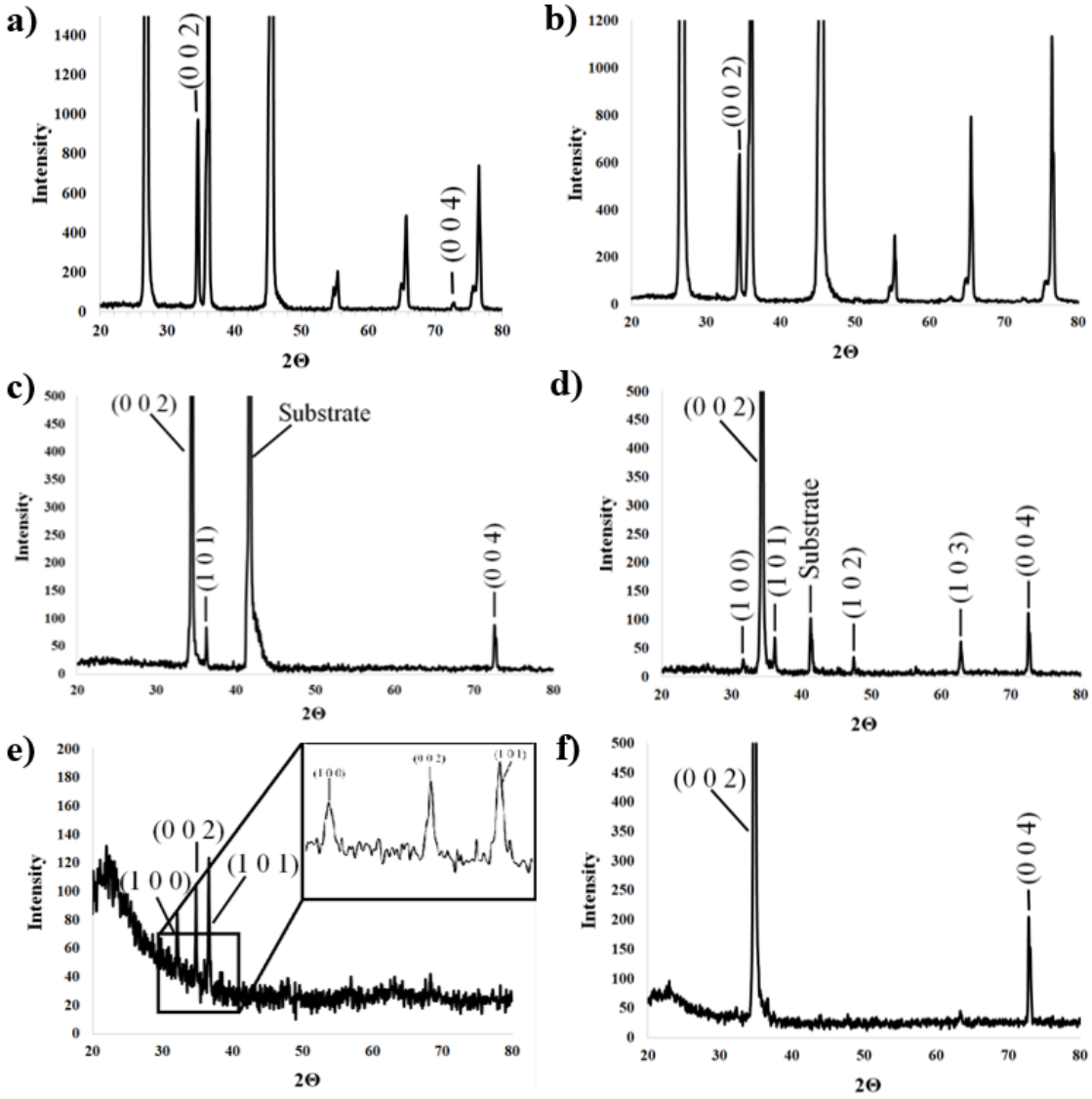


*Figure 12.* Diffractograms from powder XRD analysis of synthesized ZnO. a) bare mica substrate, b) mica substrate with ZnO seed layer, c) bare c-plane sapphire substrate, d) c-plane sapphire substrate with ZnO seed layer, e) bare fused quartz substrate, f) fused quartz substrate with ZnO seed layer.

***Room Temperature Photoluminescence***

Photoluminescence refers to the phenomenon where light is emitted from a sample after being exposed to an excitation beam of light. The energy from the excitation beam causes molecules in the sample to enter an excited state. As the molecules return to the equilibrium state, the excess energy is emitted as light. For ZnO semiconducting materials, some of the energy is involved in internal energy transitions from the valence band to the conduction band, so the type of photoluminescence observed is fluorescence. In this case, the sample emits short-lived ($10^{-8}$ to $10^{-4}$ seconds) wavelengths of light that are lower in energy, or longer wavelength, than the excitation beam. The excitation beam is typically stationary at 325 nm, and the emission detector scans from 350-600 nm.

Photoluminescence data can be used to quantify the relative number of defects in the crystal lattice of semiconductors, to understand recombination properties, and to determine the band gap of a material. Both low-temperature and room temperature photoluminescence characterization provides useful information. Analysis at low temperatures provides higher intensities and excludes interfering exchanges enabled by thermal energy at room temperature, so the properties of the material can be more accurately analyzed at low temperatures. However, these devices are typically designed to operate at room temperature or higher for practical purposes, so measuring the optical properties at room temperature can reveal the behavior of the material at functional temperatures.

When excited by 325 nm light, two types of emission bands have been reported for ZnO nanostructures: near-band emissions (NBE) and deep level emissions (DLE).

The NBE, typically observed in the UV region near the band gap of the material (380 nm or 3.37 eV), is produced by band-to-band transition and recombination of excitons formed by interaction of the sensitizing agent with photons from the light source.[30, 31] A DLE is defined as an emission observed from 400-750 nm. A broad green emission band around 500-580 nm, is typical of ZnO, but blue and yellow photoluminescence bands have also been observed in some ZnO systems.[31] The intensity of the green DLE is generally considered to be an indicator of the relative amount of oxygen vacancies or surface-level defects. The optical properties can also exhibit large variances depending on synthesis methods, shape, orientation, and size. For example, it is well-known that surface-level defects generally increase as the diameter of the nanowires decreases due to the larger accompanying surface area-to-volume ratio.[30]

The room temperature photoluminescence spectra for ZnO grown on various transparent substrates with and without ZnO seed layer application is shown in Figure 13. The NBE appears at about 400 nm for the ZnO grown on each of the substrates, which suggests the band gap of the material is approximately 3.1 eV. Energy in units of electron volts (eV) can be calculated from wavelength in meters using Equation 9 where $h$ is Planck's constant ($4.136 \times 10^{-15}$ eV*s) and $c$ is the speed of light ($3.00 \times 10^{8}$ m/s).

$$E = {}^{hc}/_{\lambda} \tag{9}$$

No significant differences in the intensity of the broad emission band were observed between the ZnO nanostructures grown on bare mica (Figure 13a) and on mica coated with a ZnO seed layer prior to growth (Figure 13b). However, the recombination band was twice as intense for the ZnO on bare mica compared to the mica substrate with a ZnO layer. Although there are drastic morphological differences in the ZnO

nanostructures grown on c-plane sapphire with and without a ZnO seed layer (Figures 9c and 9d, respectively), the room temperature photoluminescence spectra (Figures 13c and 13d, respectively) do not exhibit many differences in peak placement or intensity. The ZnO nanostructures deposited on bare fused quartz produced a room temperature photoluminescence spectrum (Figure 13e) with a considerably unique appearance compared to the other substrates. The NBE has a slightly higher intensity compared to the other spectra, but the intensity of the green emission band caused by oxygen vacancies and surface-level defects is much more prominent. This is possibly due to the nanosheet morphology of the ZnO in the sample, which would have a higher surface area, and therefore likely more surface-level defects, than the nanowires present in the other samples. Compared to Figure 13e, the ZnO nanowires grown on the fused quartz substrate treated with a ZnO seed layer produced a room temperature photoluminescence spectrum (Figure 13f) with a less intense, but a narrower, peak caused by the NBE, and the emission band indicative of defects is much less prevalent.

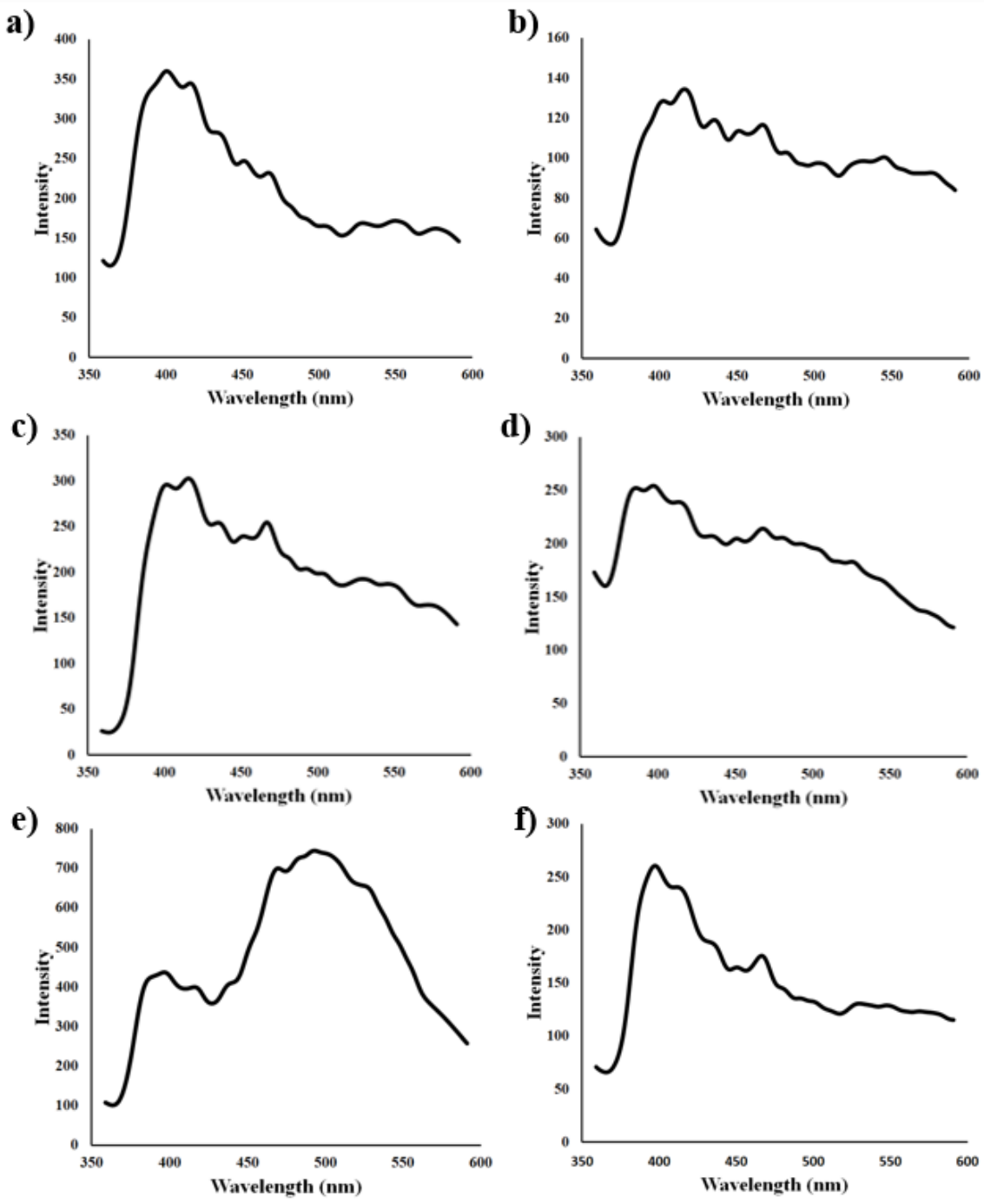


*Figure 13*. Room temperature photoluminescence spectra ZnO nanostructures of using a 325 nm excitation beam. a) bare mica substrate, b) mica substrate with ZnO seed layer, c) bare c-plane sapphire substrate, d) c-plane sapphire substrate with ZnO seed layer, e) bare fused quartz substrate, f) fused quartz substrate with ZnO seed layer.

## Conclusions

A simple method of depositing a ZnO seed layer was used to grow vertically aligned ZnO nanowires by chemical vapor deposition on fused quartz, c-plane sapphire, and mica substrates. It was shown to improve the vertical alignment and distribution of the ZnO nanostructures as opposed to ZnO nanowires grown on the same substrates excluding the ZnO seed layer. According to EDS analysis, the ratio of zinc and oxygen atomic percentages appeared to be closer to the expected 1:1 ratio on the substrates with a ZnO seed layer. XRD characterization showed growth in the direction of the (002) plane to be preferential in all the observed cases, except for growth on bare fused quartz. This sample also had more surface-level defects according to the room temperature photoluminescence data. The band gap of the ZnO on each of the substrates was approximately 3.1 eV based on the location of the near band emission at 400 nm using room temperature photoluminescence. Typically, ZnO has a band gap of 3.37, so there may be contaminants within the structures causing the band gap to be lowered. Because these experiments were not carried out in a cleanroom, the potential for contamination is much more likely.

# CHAPTER III

## Investigation of $Ga_2O_3$ Nanostructure Synthesis by Chemical Vapor Deposition using a Vapor-Liquid-Solid Mechanism

### Introduction

Preliminary studies were carried out to investigate the synthesis of $Ga_2O_3$ nanostructures using a solid precursor and a vapor-liquid-solid (VLS) method using chemical vapor deposition (CVD). Growth of nanostructures is typically catalyzed by a thin layer of metal, such as gold or silver, on the substrate surface. The catalytic layer reduces growth complications caused by lattice mismatch between the surface of the substrate and the nanostructures. A proposed mechanism for nanowire growth is illustrated in Figure 12. Vaporized metal from the solid precursor adsorbs to small droplets of gold that form as the substrate is heated (Figure 14a). Oxygen in the reaction chamber is integrated into a crystal lattice with the droplet in the center of the nanowire (Figure 14b). Since the diameter of the gold droplet decreases as the reaction progresses, tips of nanowires may be more narrow than the bases.[32]

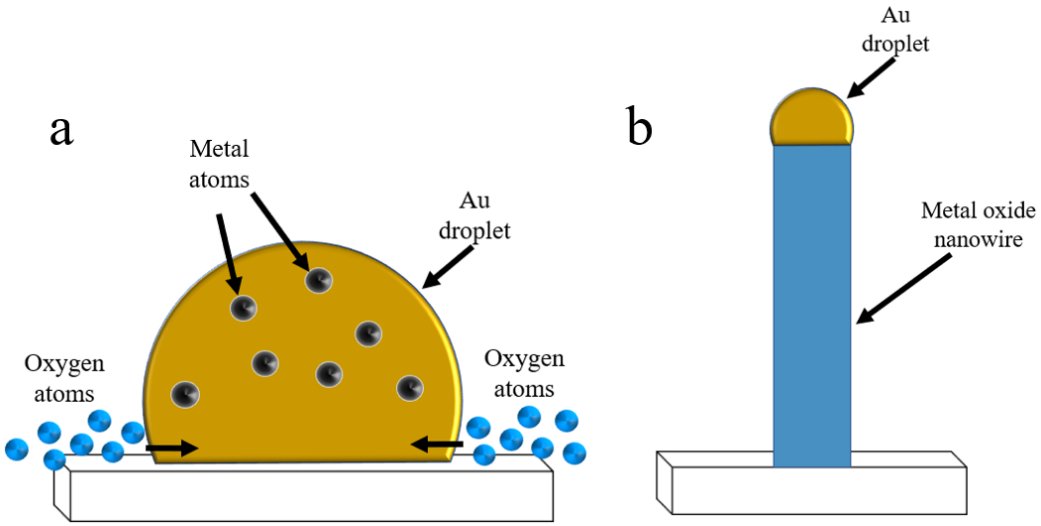


*Figure 14.* Vapor-liquid-solid growth mechanism. a) Metal atoms adsorbed to a gold droplet with oxygen atoms being incorporated into a lattice with the metal atoms at the bottom of the droplet, b) a metal oxide nanowire grown by a VLS method.

It was believed that the mechanism of growth would be similar to that proposed for ZnO with carbon being used to reduce bulk $Ga_2O_3$ to gallium and oxygen as shown in Equations 10-12.

$$Ga_2O_{3(s)} + 3C_{(s)} \rightarrow 2Ga_{(g)} + 3CO_{(g)} \quad (10)$$

$$Ga_2O_{3(s)} + 3CO_{(g)} \rightarrow 2Ga_{(g)} + 3CO_{2(g)} \quad (11)$$

$$4Ga_{(g)} + 3O_{2(g)} \rightarrow 2Ga_2O_{3(s)} \quad (12)$$

Unlike zinc, which reacts reliably as $Zn^{2+}$, there are three possible oxidation states for gallium ($Ga^{1+}$, $Ga^{2+}$, and $Ga^{3+}$); however, gallium(III) is most commonly reported in the literature. To our knowledge, no literature evidence was published regarding the multiplicity of gallium's oxidation state. It has been noted that the growth rate of $Ga_2O_3$ is considerably slower than other materials. For example, hydrothermal synthesis methods for $Ga_2O_3$ typically involve 12-hour growth times compared to growth times ranging from 3-6 hours for similar ZnO hydrothermal synthesis methods.[33, 34] The

reduction of $Ga^{3+}$ has also been shown to occur at a reduced rate compared to other metal ions because of its low redox potential.[35]

A range of nanostructures and nanoparticles were synthesized by chemical vapor deposition on Si(100) substrates with a 10-nm catalytic layer of gold under various growth conditions. The mass of solid $Ga_2O_3$/C precursor, the substrate temperature, the reaction time, and the composition of the carrier gas were among the factors that were considered. This work will be continued to develop and improve the process to reliably produce high-quality nanostructures using the CVD technique.

**Materials and Methods**

All materials and reagents were purchased from commercial sources and used without further modification. A tube furnace (OTF-1200), a gas supply system (GSL-3Z), and a vacuum pump (PV-HVS2) from MTI Corporation, Inc. were used in chemical vapor deposition experiments.

***Chemical Vapor Deposition of $Ga_2O_3$ Nanostructures***

All substrates (AU.100.SLO, Platypus Technologies) were cleaned by sonicating 10 minutes in 20 mL of ethanol (200 Proof, Sigma-Aldrich), sonicating 10 minutes in 20 mL of acetone (99.5%, VWR Chemicals), and drying under flowing $N_2$(g). The solid precursor used for CVD nanostructure synthesis was prepared by using a mortar and pestle to homogenize the appropriate amounts of $Ga_2O_3$ (99.995%, Alfa Aesar) and graphite (<20 μm synthetic, Sigma-Aldrich) to make a 1:1 molar ratio or a 1:2 molar ratio of $Ga_2O_3$ to carbon. Varied experimental factors included the substrate temperature, the growth time, and the solid precursor mass.

CVD conditions used for ZnO nanowire synthesis (Table 1) were tested for $Ga_2O_3$ nanostructure growth. Temperature intervals at the furnace edge and along the length of the quartz reaction tube were previously determined for a reaction temperature of 950°C. Temperatures were recorded at 0.5 cm intervals relative to the end of the insulation on the right side of the furnace. For the experiments that were not carried out with the reaction tube in the center of the tube furnace, the middle substrate (substrate B) was placed 3.5 cm to the left of the end of the insulation as shown in Figure 15. Three Si(100) substrates with a 10 nm catalytic layer of gold were used in each experiment for deposition over a wider temperature range.

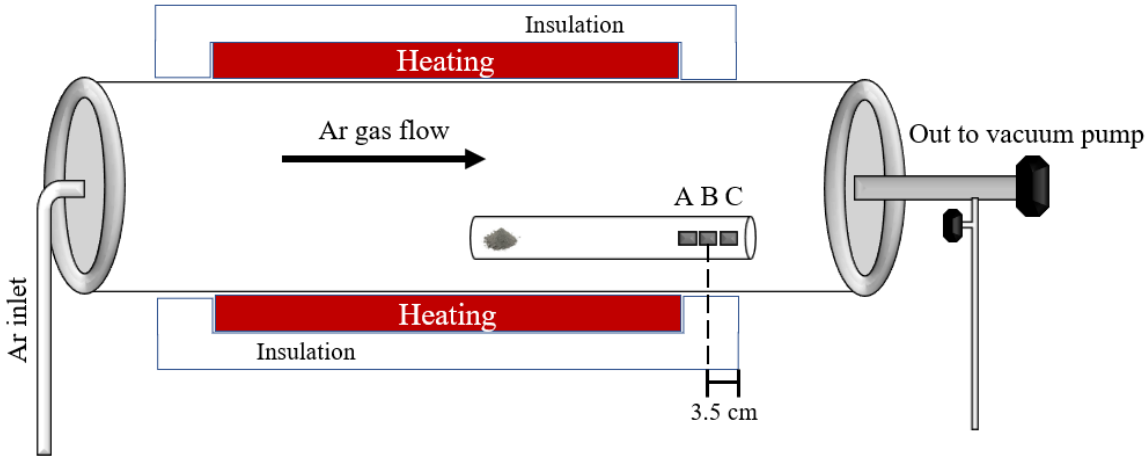


*Figure 15.* Tube furnace used for CVD synthesis of $Ga_2O_3$ nanostructures.

The role of the precursor mass was studied using the conditions in Table 4. The molar ratio of $Ga_2O_3$ to carbon was 1:1, and the mass of the precursor was varied from 50-150 mg. The effect of reaction times of 60, 75, and 90 minutes was studied with 75 mg of solid precursor under the conditions in Table 4. 150 mg of was used in a 90-minute reaction with $O_2$(g) at a flow rate of 1 $cm^3$/min added to the 80 $cm^3$/min flow of Ar(g).

*Table 4*. Experimental $Ga_2O_3$ CVD conditions in the center of the tube furnace.

| Experimental Parameters | Conditions |
|---|---|
| Pressure | 3.4 hPa (2.55 Torr) |
| Gas flow | 80 $cm^3$/min $Ar_{(g)}$ |
| Reaction temperature | 950°C |
| Heating rate | 10°C/min |
| Substrate temperature | 950°C |

A 50 mg sample and a 75 mg sample of a precursor with a 1:2 ratio of $Ga_2O_3$ to carbon was used in separate experiments carried out under the conditions in Table 5.

*Table 5*. Experimental conditions for CVD of $Ga_2O_3$ with substrate at 730ºC.

| Experimental Parameters | Conditions |
|---|---|
| Pressure | 3.4 hPa (2.55 Torr) |
| Gas flow | 80 $cm^3$/min $Ar_{(g)}$ |
| Reaction temperature | 950°C |
| Heating rate | 10°C/min |
| Substrate temperature | 730ºC |

***Characterization of Nanoparticles and Nanostructures***

The samples were characterized using scanning electron microscopy (SEM, Hitachi SU3500) and energy dispersive X-ray spectroscopy (EDS). From SEM images, the size and shape of the structures were visualized. EDS data provided an estimate of the mass percentages of gallium and oxygen in the sample. The mass percentages of gallium and oxygen obtained by EDS analysis were converted to atomic percentages using Equations 13 and 14.

$$atomic\%\ of\ Ga = \frac{\frac{mass\%\ Ga}{MW\ Ga}}{\frac{mass\%\ Ga}{MW\ Ga} + \frac{mass\%\ O}{MW\ O}} \quad (13)$$

$$atomic\%\ of\ O = \frac{\frac{mass\%\ O}{MW\ O}}{\frac{mass\%\ Ga}{MW\ Ga} + \frac{mass\%\ O}{MW\ O}} \quad (14)$$

**Results and Discussion**

Overall, nanoparticles were the most common product formed on the Si(100) substrates with a catalytic 10 nm Au layer. Because of sparse deposition onto the substrates, comprehensive X-ray diffraction (XRD) data was difficult to obtain using the powder XRD instrumentation intended for analysis of bulk samples. Room temperature photoluminescence data from the samples was also not possible to obtain using the available instrument. At this time, SEM images and EDS data were used to characterize the morphology and average atomic composition of the products.

The nanostructures and nanoparticles shown in Figure 16 were produced using a 50 mg precursor with a 1:1 ratio of $Ga_2O_3$ to carbon under the conditions described in Table 4 in the Methods section for a 60-minute reaction time. The type of deposition appeared to depend on the proximity of the substrate to the precursor material. More tube-like nanostructures were deposited on substrate A (Figure 16a) than substrates B (Figure 16b) and C (Figure 16c) which seemed to have more particle deposition. The substrates are shown in Figure 16d to indicate the differences in visible appearance as well.

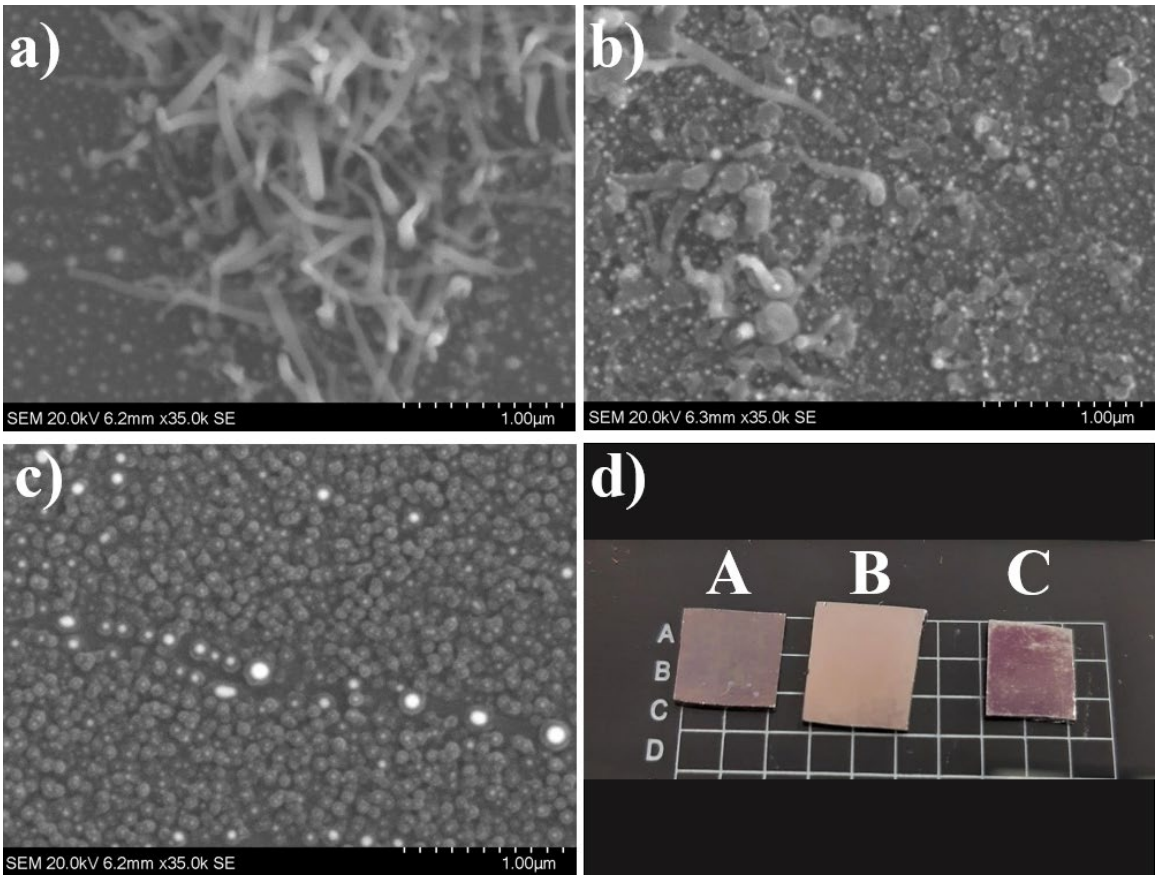


*Figure 16.* SEM images of nanostructures and nanoparticles synthesized with $Ga_2O_3$ and graphite precursor.

The experiment was repeated, but a different deposition was observed (Figure 17a). The SEM images of substrates produced at 60-, 75-, and 90-minute reaction times when the mass of the precursor was increased to 75 mg and experiments were conducted under the conditions in Table 5 are shown in Figure 17b, Figure 17c, and Figure 17d, respectively. There appears to be an increase in deposition that correlates positively with reaction time; however, the darker part of the particles seems to grow more than the light centers. The diameters of the particles produced with the 60-minute reaction time with 75 mg of precursor ranged from 30 to 50 nm, but EDS analysis did not detect significant amounts of gallium or oxygen in the sample. The 75-minute reaction time produced particles with diameters ranging from 20-70 nm with an average atomic composition of

100% oxygen. The 90-minute reaction time yielded particles with an average diameter of 85 nm, but the average atomic composition was also found to be 100% oxygen by EDS analysis. It is believed that these likely are Au nanoislands formed from the catalytic layer.

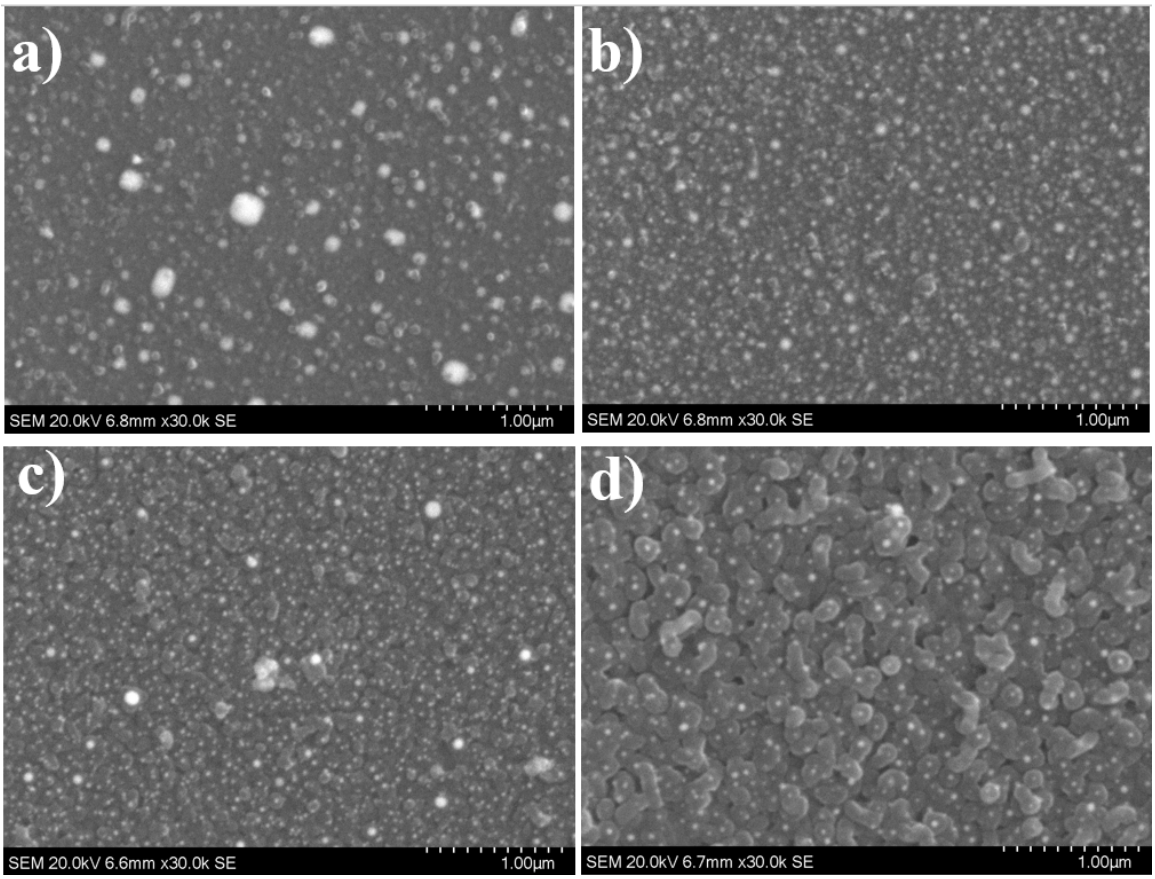


*Figure 17.* Effect of reaction time on $Ga_2O_3$ deposition. a) 50 mg precursor for 60 minutes, b) 75 mg precursor for 60 minutes, c) 75 mg precursor for 75 minutes, d) 75 mg precursor for 90 minutes.

Figure 18 shows the deposition achieved by increasing the precursor to 150 mg and introducing $O_{2(g)}$ into the argon carrier gas. Nanoparticles ranging in diameter from 30-200 nm were deposited on substrate A (Figure 18a). The lighter centers of these particles ranged from 45-285 nm in diameter and were surrounded by a darker ring which added 70-110 nm to the total diameter of the particle. The ratio of the lighter particle

center to the surrounding ring increased as the total particle size increased. Substrate B (Figure 18b) showed particle nucleation with random, sparse tubelike nanostructure growth. Substrate C (Figure 18c) showed particles with an average diameter of 100 nm with a few larger particles 580 nm in diameter. The cause for this halo effect around the particles is unknown.

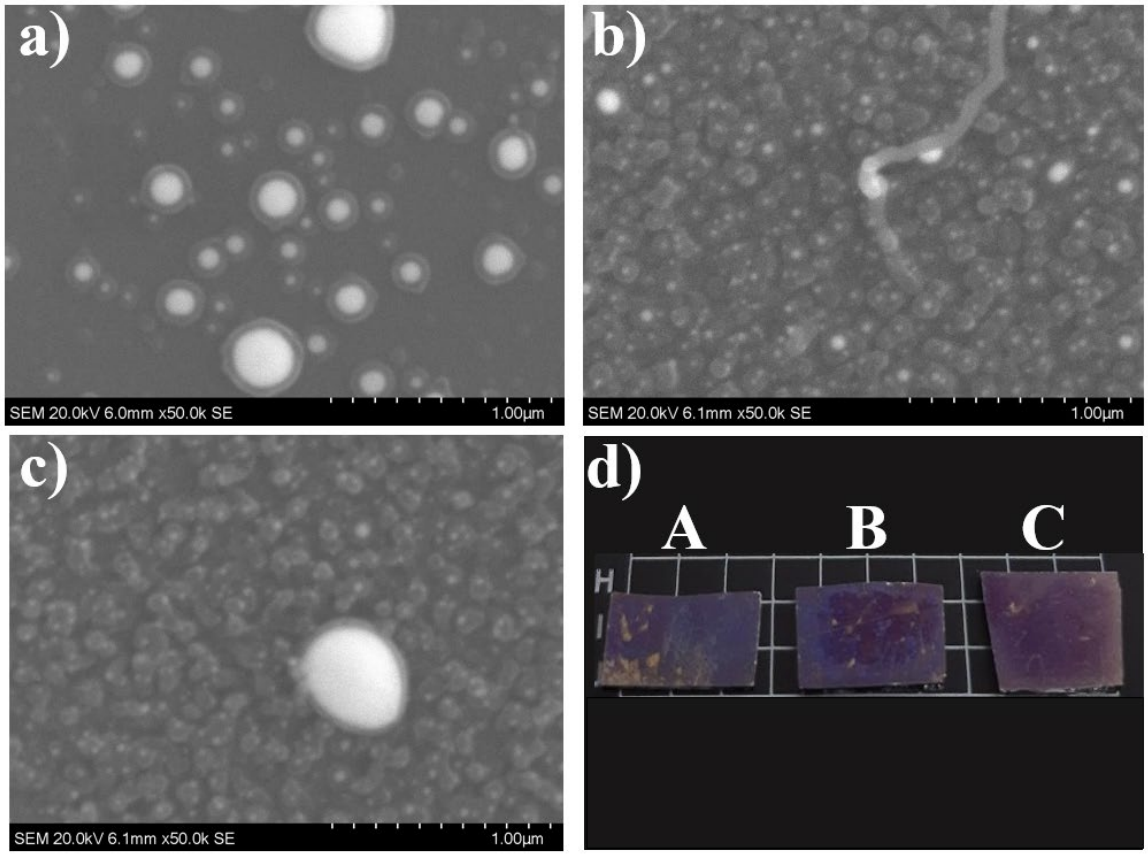


*Figure 18.* Effect of oxygen incorporated into the carrier gas.

The average atomic percentages for each substrate are reported in Table 6. From this data, the identity of the product cannot be determined. Further analysis by XRD and Raman spectroscopy techniques will be necessary in the future.

*Table 6.* Average atomic composition of products formed at 950°C.

| Figure | Ga atomic% | O atomic% |
|---|---|---|
| 16a | 0 | 100 |
| 16b | 19 | 81 |
| 16c | 0 | 0 |
| 17a | 15 | 85 |
| 17b | 0 | 0 |
| 17c | 0 | 100 |
| 17d | 0 | 100 |
| 18a | 2 | 98 |
| 18b | 100 | 0 |
| 18c | 76 | 24 |

Thin wire-like structures, shown in Figure 19, were obtained using a 50 mg precursor with a 1:2 ratio of $Ga_2O_3$ to carbon under the conditions in Table 5 in the Methods section. However, these results have not been able to be reproduced at this time. The deposition was more concentrated on substrate A (Figure 19a), which was closer to the precursor material and consistent with the previous experiments. This is likely caused by increased nucleation on the surface of the closest substrate which would encourage more growth. Substrate C had substantially less product deposition with nanoparticles approximately 30 nm in diameter.

Visible differences in deposition could be observed on the substrates as shown in Figure 19d with a more prevalent film on substrate A than on substrate B and a thicker film on substrate B compared to substrate C. The color of the substrates reacted at 730°C also changed to white with a blue tint compared to the pink and purple shades of the samples reacted at 950°C. The EDS data for these samples revealed the ratios of gallium to oxygen to be approximately 2:3 for substrate A and about 1:1 for substrates B and C.

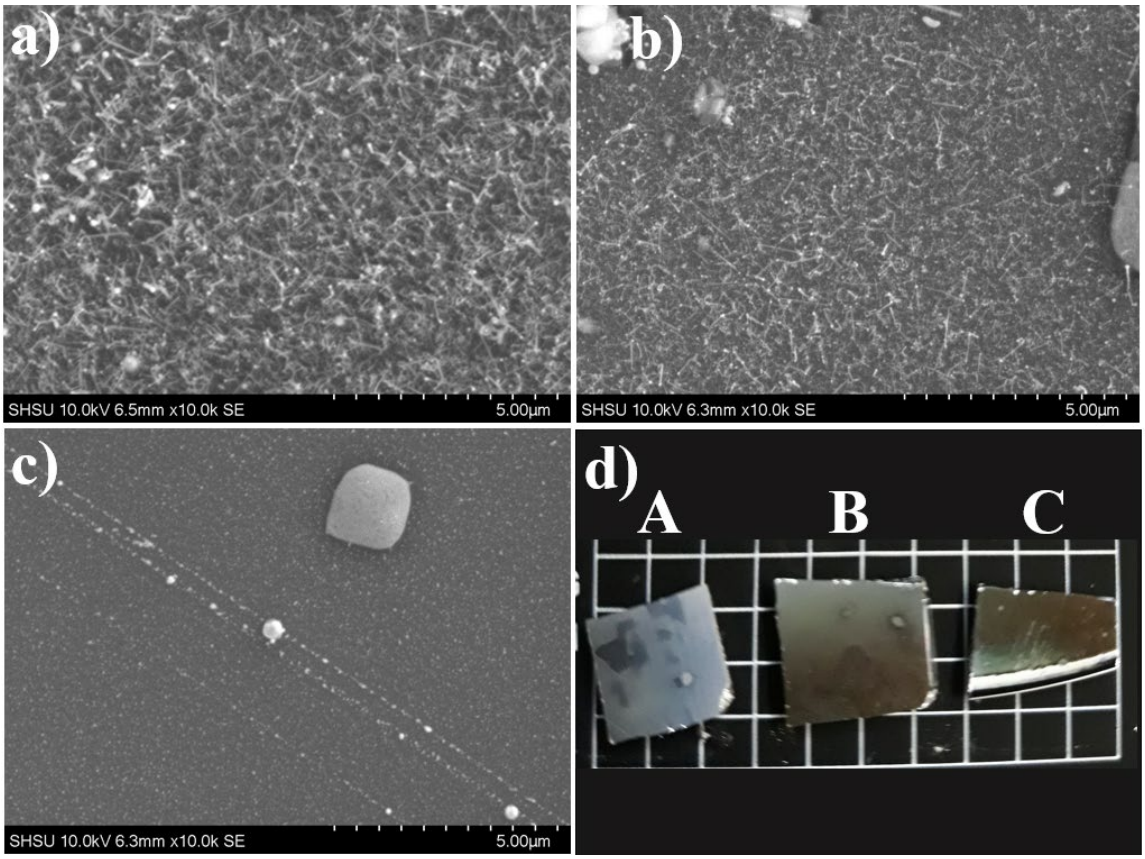


*Figure 19.* Nanostructures grown with a 1:2 ratio of $Ga_2O_3$ to carbon precursor (50 mg) at 730°C.

When the experiment was repeated with a 75 mg precursor with a 1:2 ratio of $Ga_2O_3$ to carbon under the same conditions (Table 5), nanoparticles (Figure 20), rather than the wire-like structures, nanoparticles were produced. The distribution of deposition and the size of the nanoparticles deposited on substrates A (Figure 20a) and B (Figure

20b) was similar, but the deposition on substrate C (Figure 20c) resulted in much smaller nanoparticle formation. Looking at the substrates (Figure 20d), the areas of the substrates with a color change to green are irregularly shaped and unevenly distributed on the substrate.

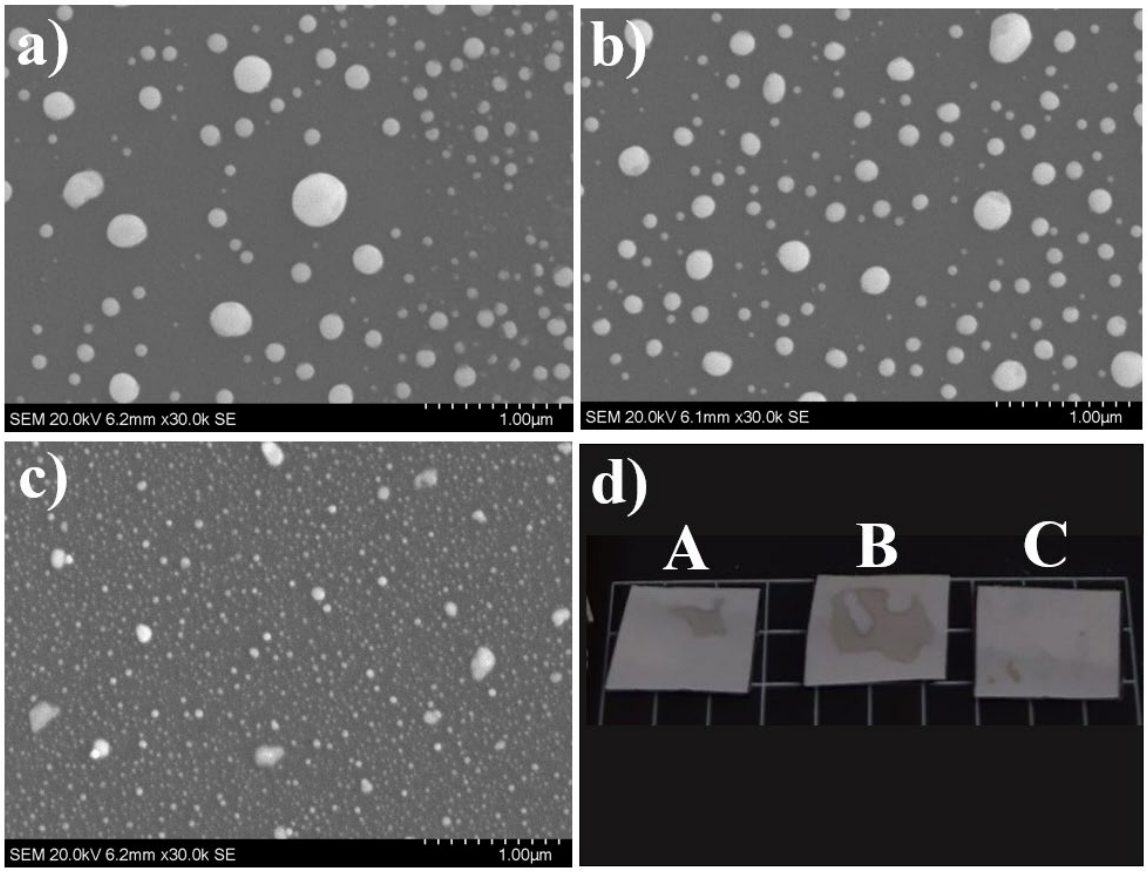


*Figure 20.* Nanoparticles grown with a 1:2 ratio of $Ga_2O_3$ to carbon precursor (75 mg) at 730°C.

The average atomic compositions of the nanostructures produced at 730°C using different masses of a precursor with a 1:2 ratio of $Ga_2O_3$ to carbon (Figures 19 and 20) are reported in Table 7. Data from EDS analysis of the substrates in Figure 20 suggested that no significant amount of gallium or oxygen was detected on substrates A and C. The

ratio of the average atomic percentages of gallium and oxygen on substrate B was approximately 1:1.

*Table 7*. Average atomic composition of products formed at 730°C.

| Figure | Ga atomic% | O atomic% |
|---|---|---|
| 19a | 37 | 63 |
| 19b | 55 | 45 |
| 19c | 47 | 53 |
| 20a | 0 | 0 |
| 20b | 54 | 46 |
| 20c | 0 | 0 |

**Conclusions**

The effects of reaction time, precursor mass, carrier gas composition, and substrate temperature were investigated for the synthesis of $Ga_2O_3$ nanostructures by CVD. The amount of deposition was shown to increase with longer reaction times. The effects of the precursor mass and carrier gas composition could not be conclusively determined at this time because of the lack of reproducibility of the results for many of the experiments. Substrate temperature appeared to have a noticeable effect on the visible color changes of the substrate, but both nanostructures and nanoparticles were formed in the two temperature zones. However, the wire-like structures have not been replicated. EDS analysis of the structures provided inconclusive information about the composition of the structures formed on many of the substrates, but most of them appear to be oxygen rich. This might suggest that the concentration of gallium in the transported vapor is too low, possibly caused by the slow reduction rate of $Ga^{3+}$ ions, which would

cause inadequate growth and account for the high oxygen percentages in the sample. Some procedures are known to use gallium metal in addition to $Ga_2O_3$ as a precursor.[36] Because of the sparse nature of the deposition, the identity of the product has not been determined using XRD, Raman spectroscopy, or room temperature photoluminescence. Since the precursor only contains $Ga_2O_3$ and graphite, it is assumed that the product would be $Ga_2O_3$ or possibly GaOOH. Further studies must be completed to make these conclusions. Reaction pressure and gas flow variation should also be explored in the future.

# CHAPTER IV

## Investigation of Dye-sensitized Solar Cell Construction and Testing

### Introduction

Dye-sensitized solar cells can be constructed in many ways using the five basic components: a working electrode, a semiconductive material, a photoactive sensitizing agent, an electrolyte, and a counter electrode. With many options for each component, it is important to have a standard way to test cells to objectively compare power conversion efficiencies of cells constructed by different methods. The American Society for Testing and Materials (ASTM) has set guidelines for standardized testing of solar cells based on their application.[37, 38] The air mass spectrum of light, the amount of irradiance, the cell temperature, and the type of probe used to collect measurements.

In solar energy applications, the air mass coefficient (AM) is based on the path length of light to the location. An air mass coefficient of 1 occurs when the sun is directly overhead at sea level. The direct overhead position of the sun is referred to as the zenith. As the location of the sun shifts farther from overhead, the zenith angle as well as the path length of the light increases (Figure 21).[38] The ratio of the path length of light at different angles to the path length at the zenith is the air mass coefficient. The suffix "G" (global) after the air mass coefficient indicates diffuse and scattered light is included in the spectrum. The suffix "D" (direct) applies to a spectrum that does not include reflections or scattered light. AM1.5G is the standard spectrum of light for testing photovoltaic devices because it corresponds to the latitudes of many of the largely populated areas in the world based on a yearly average.[38] In addition to the spectrum, the

amount of irradiance used in standard tests is referred to as “one sun” which is equivalent to 1000 W/m$^2$, or 100 mW/cm$^2$.

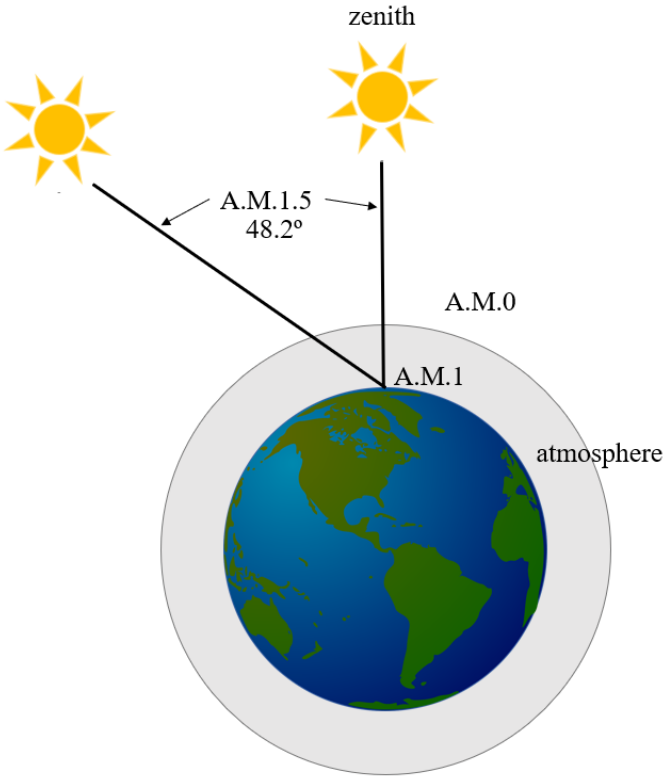


*Figure 21.* Illustration of air mass coefficients.[2]

Four-wire measurements are required for DSSC testing because they provide the most accurate electronic data for the cell. Kelvin probes consist of two wires connected to a voltmeter and two wires connected to an ammeter. These are isolated from each other to reduce the effects of the resistance of the probes by ensuring current from the ammeter does not interfere with the voltage readings and vice versa. Iterations are required to record many measurements for the cell when variable loads are applied to determine the current and voltage under a variety of circumstances.[39] The IV curve is produced from these measurements where the short-circuit current occurs when the voltage is 0, and the open-circuit voltage corresponds to the voltage when the current is 0.

The current and voltage at maximum power are also significant properties of the cell obtained from the IV curve.

Procedures for simple dye-sensitized solar cells (DSSC) have been written for use in introductory chemistry courses using relatively common laboratory materials and equipment and often using fruit juice as the source of a photoactive dye.[40, 41] Rudimentary cells based on colloidal $TiO_2$ were made and tested as part of the preliminary studies in our lab to form a foundational understanding for making and testing DSSCs. These cells were made using indium-doped tin oxide (ITO) conductive glass, $TiO_2$ paste, a photoactive dye, an $I^-/I_3^-$ electrolyte solution, and ITO conductive glass coated with graphite (Figure 22).

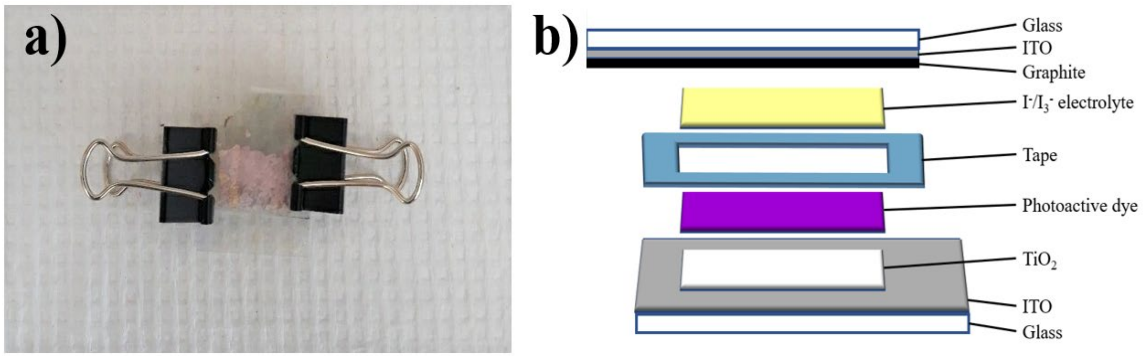


*Figure 22.* Rudimentary dye-sensitized solar cell design. a) Photograph of a DSSC based on colloidal $TiO_2$. b) Diagram showing the layers of the DSSC.

## Materials and Methods

### *Preparation of ITO Conductive Glass*

A previously existing procedure[42] for producing surface conductive glass was modified and used to make conductive glass by depositing an ITO layer. A 5 g sample2 of $SnCl_4$ (98+%, Acros Organics) was fully dissolved in 5 mL of methanol with vortexing in a small glass vial. In a separate vial, 0.1 g of indium nitrate hydrate (99%, Sigma-Aldrich) was dissolved in 3 mL of HCl and diluted with 17 mL of methanol to

form a total of 20 mL of the solution. The final ITO spray solution was prepared by mixing 4 mL of the indium nitrate solution with 5 mL of the $SnCl_4$ solution. A few mL of the solution were transferred to a vial fitted with a clean atomizer originally meant to dispense a fragrance such as cologne.

Glass microscope slides were cut into thirds to create three glass substrates (1-inch x 1-inch). The glass substrates were cleaned by sonicating for 10 minutes in ethanol followed by sonication in acetone and drying under flowing $N_2(g)$. The substrates were heated at 600°C for 15 minutes in a small oven located inside a fume hood. The substrates were carefully removed completely and immediately sprayed with the ITO solution for 15-20 seconds. An aluminum foil backdrop was used to prevent overspray from settling onto other equipment in the fume hood. The substrates were placed in the oven and heated at 600°C for 2.5 minutes, removed from the oven, sprayed again with the ITO solution, and heated at 600°C for an additional 2.5 minutes. Finally, they were allowed to cool to room temperature before testing the surface conductivity using a multimeter on the resistance setting. The positive and negative electrodes were placed on the glass near each other, but without directly touching. If the surface was conductive, the resistance dropped from essentially infinite, as in the case of untreated glass, to near 0 Ω (1-3 Ω) for glass with a conductive ITO layer.

***DSSC Construction***

DSSCs were fabricated using a slightly modified procedure reported by Smestead and Grätzel.[40] A small amount of $TiO_2$ was mixed with dilute nitric acid to make a paste with a consistency similar to wet paint. A rectangle was taped off in the middle of the glass substrate on the side coated with ITO. A small amount of the prepared $TiO_2$ paste

was placed on one side inside the taped-off area and pushed across the entire area with a glass stirring rod. The tape border was removed, and the paste was dried at room temperature for 10 minutes before being annealed on a hot plate at 450°C for 30 minutes.

Once the substrate had cooled to room temperature, the annealed $TiO_2$ was covered with the N3 dye solution. A 0.9 mM solution of N3 dye was made by dissolving 0.0126 g of N3 dye (cis-bis(isothiocyanato)bis(2,2′-bipyridyl-4,4′-dicarboxylato)ruthenium(II), Sigma-Aldrich) in 20 mL of ethanol (200 proof, Sigma-Aldrich). The structure of the dye is shown in Figure 23.

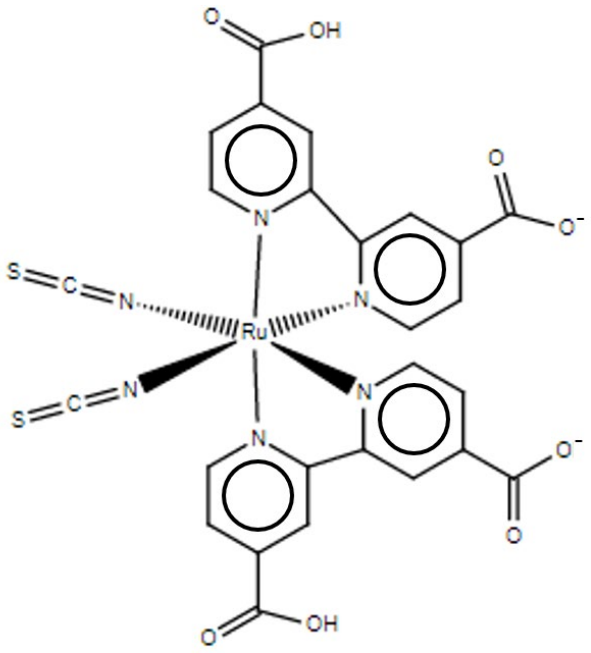


*Figure 23.* Structure of N3 dye.

After allowing the dye to adsorb to the $TiO_2$ for 10-30 minutes, the working electrode was rinsed with deionized water, rinsed with acetone, and dried at room temperature for 10 minutes to ensure it was completely dry. Tape was applied around the $TiO_2$ area to act as a barrier between the conductive glass substrates to prevent short-circuiting of the device (Figure 24).

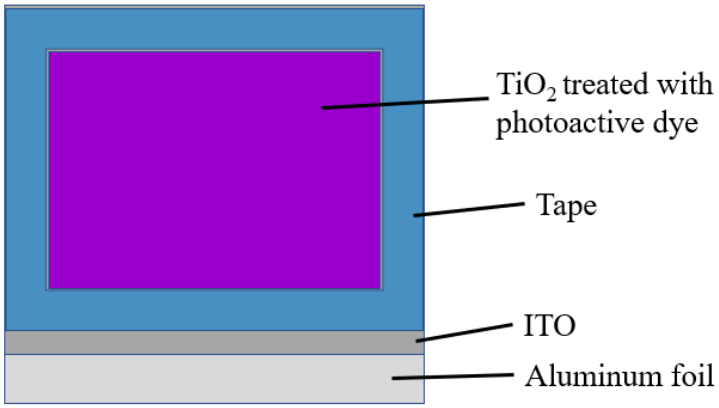


*Figure 24.* A diagram of the working electrode of the DSSC.

The conductive side of the counter electrode was coated with graphite from a soft pencil (2B). The $I^-/I_3^-$ electrolyte solution was 0.5 mM $I_2$ and 0.5 M KI in ethylene glycol. One drop of the electrolyte solution was place on the dyed $TiO_2$, and the graphite-covered side of the counter electrode was secured on top with binder clips in an offset fashion to allow alligator clips to be attached to each electrode for testing. Aluminum foil (in place of copper foil) was folded over the area of both electrodes where the clip would be attached.

***DSSC Testing***

Current and voltage measurements were taken for the DSSCs under simulated sunlight (G2V Pico LED) using a multimeter. The G2V Pico IV module was used to test the DSSC following the ASTM E1021 standard methods for testing terrestrial

photovoltaic devices: air mass 1.5 spectrum (AM1.5G), one-sun of illumination ($100 mW/cm^2$), temperature of 25°C, and four-wire measurements to remove interference from resistance caused by contact of the probe with the cell.[38] The positive (red) electrode was connected to the counter electrode (graphite-coated) of the cell, and the negative (black) electrode was attached to the working electrode to take measurements from 1 to -1 V at a step size of -0.1.

**Results and Discussion**

Although the concentrations of $SnCl_4$ and indium nitrate in the solution were reduced, ITO-coated conductive glass with a surface resistance of 1-4 Ω was produced when the probes were touching the surface 0.5 cm apart. However, it was observed that the resistance increased over time as the conductive glass was used as an electrode.

***Reference Cell***

The reference cell, shown in Figure 25, was tested using four-wire measurements and the pre-loaded parameters in the G2V IV module.

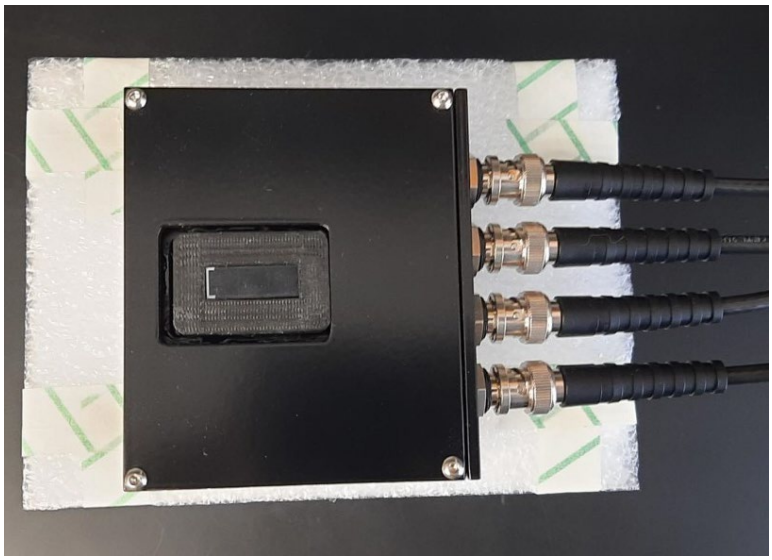

*Figure 25*. Photo of the reference cell.

However, unlike the Kelvin probe used to test the fabricated DSSC, the wires were directly connected to the cell without the need for additional clips. The generated IV curve is shown in Figure 26, and the properties of the cell are reported in Table 8.

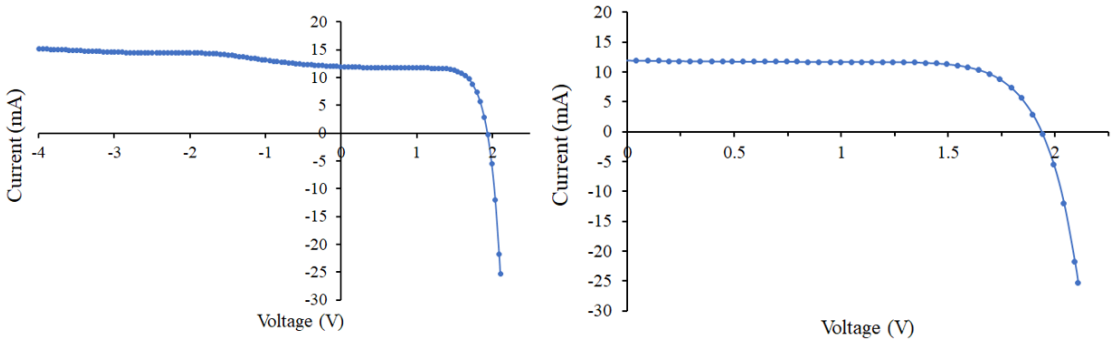


*Figure 26.* IV curve produced by the G2V reference cell.

*Table 8.* Measured and calculated properties of the reference cell.

| Property | Value |
|---|---|
| **Efficiency** | 18.05% |
| **$V_{OC}$** | 1.937 V |
| **$I_{SC}$** | 11.95 mA |
| **$I_M$** | 10.82 mA |
| **$V_M$** | 1.592 mA |
| **FF** | 74.46% |

### *Fabricated DSSC Based on Bulk $TiO_2$*

Proper execution when fabricating a solar cell affects the performance of the cell perhaps as much as the components of the cell. The consistency of the $TiO_2$ paste was shown to have a large effect on its ability to correctly anneal to the glass substrate. It was

also noted that the ethanol-based dye solution appeared to begin weakening the annealed $TiO_2$ layer, and the solvent evaporated before the adsorption time was complete. When fruit juice is used as the dye source, the solvent is water-based, so it is able to cover the surface for more time without breaking down the $TiO_2$ layer.

Using a multimeter with regular alligator clips to measure the current and voltage of the cell under simulated light (AM1.5G) at a 1 cm working distance (Figure 24), the maximum recorded current was 10 μA and the maximum voltage was 361 mV. The literature suggests that for a cell of this size using blackberry juice as the source of photoactive anthocyanin dyes, a current of 3-4 mA should be achieved.[40] The ability of electrons to flow through the cell are highly dependent on the conductive nature of the ITO layer, and it was noted that the stability of the synthesized ITO layer was not consistent over time.

The same cell was then tested under the same conditions using the G2V IV module. However, there was difficulty in attaching the clips of the Kelvin probe to the cell in a way that ensured a stable connection. To get readings, ordinary alligator clips were required to connect the two clips of the Kelvin probe to the DSSC (Figure 27).

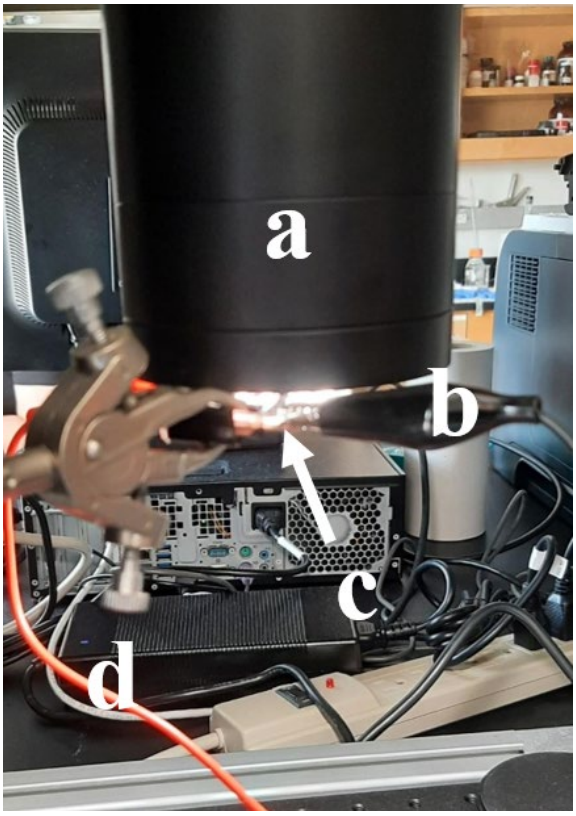


*Figure 27.* Fabricated DSSC at a 1 cm working distance from the solar simulator. a) Solar simulator, b) negative electrode, c) fabricated DSSC under simulated sunlight, d) positive electrode.

Three trials showed consistent data for the cell. The obtained data (Figure 28) appeared in a stepwise manner rather than in the shape of a typical IV curve, but it was consistent for each of the three trials. The measured and calculated properties of the DSSC trials are shown in Table 9.

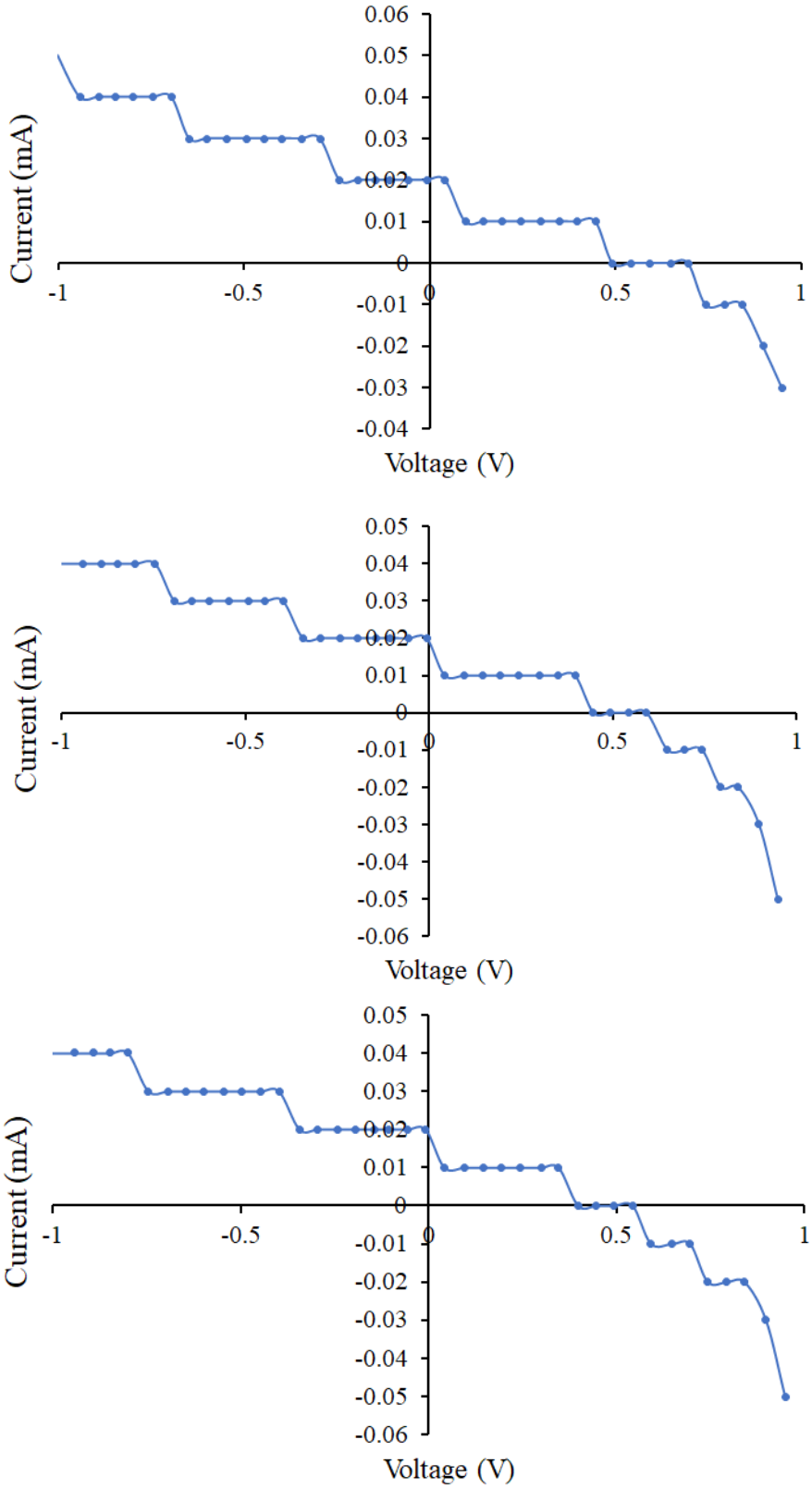


*Figure 28.* Three trials of a DSSC based on bulk $TiO_2$ with N3 dye and $I^-/I_3^-$ electrolyte solution.

*Table 9.* Properties of the DSSC based on bulk $TiO_2$ with N3 dye and $I^-/I_3^-$ electrolyte.

| Property | Trial 1 | Trial 2 | Trial 3 |
|---|---|---|---|
| **Efficiency** | 0.01% | 0.01% | 0.01% |
| **$V_{OC}$** | 0.543 V | 0.592 V | 0.543 V |
| **$I_{SC}$** | 0.02 mA | 0.02 mA | 0.02 mA |
| **Maximum current** | 0.01 mA | 0.01 mA | 0.01 mA |
| **Maximum voltage** | 0.346 mA | 0.397 V | 0.346 V |
| **FF** | 34.63% | 36.11% | 34.63% |

The open-circuit voltage was comparable to the reported range (0.3-0.5 V) for this category of DSSCs, but the short-circuit current was significantly lower than the expected 3-4 mA.[40] This insufficient flow of current may have been caused by the deterioration of the ITO conductive layers on the electrodes or the quality of the $TiO_2$ film.

**Conclusions**

The IV module of the solar simulator was shown to be capable of producing a typical IV curve using a reference cell purchased from the manufacturer of the solar simulator. The clips of the Kelvin probe used to analyze the fabricated cell formed inferior connections with the cell, which was believed to be a possible source of error in the measurements. The quality of the ITO layer may have hindered the flow of current through the DSSC, so a DSSC using commercially available ITO conductive glass substrates should be tested to determine whether the method used to prepare the conductive glass in the lab is viable for this application. An ethylene glycol dye solution rather than ethanol may better maintain the integrity of the $TiO_2$ layer while allowing the dye to adsorb to the layer without solvent evaporation.

## REFERENCES


1. O'Regan, B.; Grätzel, M., *Nature* **1991,** *353* (6346), 737-740.
2. Chen, C.-Y.; Wang, M.; Li, J.-Y.; Pootrakulchote, N.; Alibabaei, L.; Ngoc-le, C.-h.; Decoppet, J.-D.; Tsai, J.-H.; Grätzel, C.; Wu, C.-G.; Zakeeruddin, S. M.; Grätzel, M., *ACS Nano* **2009,** *3* (10), 3103-3109.
3. Horiuchi, T.; Miura, H.; Sumioka, K.; Uchida, S., *Journal of the American Chemical Society* **2004,** *126* (39), 12218-12219.
4. Zhang, L.; Yang, X.; Wang, W.; Gurzadyan, G. G.; Li, J.; Li, X.; An, J.; Yu, Z.; Wang, H.; Cai, B.; Hagfeldt, A.; Sun, L., *ACS Energy Letters* **2019,** *4* (4), 943-951.
5. Karthikeyan, S.; Lee, J. Y., *The Journal of Physical Chemistry A* **2013,** *117* (42), 10973-10979.
6. Yella, A.; Lee, H.-W.; Tsao, H. N.; Yi, C.; Chandiran, A. K.; Nazeeruddin, M. K.; Diau, E. W.-G.; Yeh, C.-Y.; Zakeeruddin, S. M.; Grätzel, M., *Science* **2011,** *334* (6056), 629.
7. Mathew, S.; Yella, A.; Gao, P.; Humphry-Baker, R.; Curchod, B. F. E.; Ashari-Astani, N.; Tavernelli, I.; Rothlisberger, U.; Nazeeruddin, M. K.; Grätzel, M., *Nature Chemistry* **2014,** *6* (3), 242-247.
8. Wang, J.; Mora-Seró, I.; Pan, Z.; Zhao, K.; Zhang, H.; Feng, Y.; Yang, G.; Zhong, X.; Bisquert, J., *Journal of the American Chemical Society* **2013,** *135* (42), 15913-15922.
9. Pan, Z.; Rao, H.; Mora-Seró, I.; Bisquert, J.; Zhong, X., *Chemical Society Reviews* **2018,** *47*, 7659-7702.

10. Yu, J.; Wang, W.; Pan, Z.; Du, J.; Ren, Z.; Xue, W.; Zhong, X., *J. Mater. Chem. A* **2017,** *5*, 14124-14133.

11. Yoon, H.; Kang, S.; Lee, J.-K.; Choi, M., *Energy Environ. Sci.* **2016,** *9*, 2262-2266.

12. Sahli, F.; Werner, J.; Kamino, B. A.; Bräuninger, M.; Monnard, R.; Paviet-Salomon, B.; Barraud, L.; Ding, L.; Diaz Leon, J. J.; Sacchetto, D.; Cattaneo, G.; Despeisse, M.; Boccard, M.; Nicolay, S.; Jeangros, Q.; Niesen, B.; Ballif, C., *Nature Materials* **2018,** *17* (9), 820-826.

13. Boschloo, G.; Hagfeldt, A., *Accounts of Chemical Research* **2009,** *42* (11), 1819-1826.

14. O'Regan, B. C.; Durrant, J. R., *Accounts of Chemical Research* **2009,** *42* (11), 1799-1808.

15. Pelet, S.; Moser, J.-E.; Grätzel, M., *The Journal of Physical Chemistry B* **2000,** *104* (8), 1791-1795.

16. Kubo, W.; Kambe, S.; Nakade, S.; Kitamura, T.; Hanabusa, K.; Wada, Y.; Yanagida, S., *The Journal of Physical Chemistry B* **2003,** *107* (18), 4374-4381.

17. Feng, W.; Zhao, L.; Du, J.; Li, Y.; Zhong, X., *J. Mater. Chem. A* **2016,** *4*, 14849-14856.

18. Cao, Y.; Saygili, Y.; Ummadisingu, A.; Teuscher, J.; Luo, J.; Pellet, N.; Giordano, F.; Zakeeruddin, S. M.; Moser, J. E.; Freitag, M.; Hagfeldt, A.; Grätzel, M., *Nature Communications* **2017,** *8* (1), 15390.

19. Yuhas, B. D.; Yang, P., *Journal of the American Chemical Society* **2009,** *131* (10), 3756-3761.

20. Pradel, K. C.; Wu, W.; Zhou, Y.; Wen, X.; Ding, Y.; Wang, Z. L., *Nano Letters* **2013,** *13* (6), 2647-2653.

21. Yuan, G. D.; Zhang, W. J.; Jie, J. S.; Fan, X.; Zapien, J. A.; Leung, Y. H.; Luo, L. B.; Wang, P. F.; Lee, C. S.; Lee, S. T., *Nano Letters* **2008,** *8* (8), 2591-2597.

22. Suja, M.; Bashar, S. B.; Morshed, M. M.; Liu, J., *ACS Applied Materials & Interfaces* **2015,** *7* (16), 8894-8899.

23. Law, M.; Greene, L. E.; Johnson, J. C.; Saykally, R.; Yang, P., *Nature Materials* **2005,** *4* (6), 455-459.

24. Bakr, Z. H.; Wali, Q.; Yang, S.; Yousefsadeh, M.; Padmasree, K. P.; Ismail, J.; Ab Rahim, M. H.; Yusoff, M. M.; Jose, R., *Industrial & Engineering Chemistry Research* **2019,** *58* (2), 643-653.

25. Wang, S.; Chen, K.; Zhao, H.; He, C.; Wu, C.; Guo, D.; Zhao, N.; Ungar, G.; Shen, J.; Chu, X.; Li, P.; Tang, W., *RSC Advances* **2019,** *9* (11), 6064-6069.

26. Wang, G.; Park, J.; Kong, X.; Wilson, P. R.; Chen, Z.; Ahn, J.-h., *Crystal Growth & Design* **2008,** *8* (6), 1940-1944.

27. Kumar, S.; Tessarek, C.; Sarau, G.; Christiansen, S.; Singh, R., *Advanced Engineering Materials* **2015,** *17* (5), 709-715.

28. Rafique, S.; Han, L.; Zorman, C. A.; Zhao, H., *Crystal Growth & Design* **2016,** *16* (1), 511-517.

29. Drago, R. S., *Physical Methods For Chemists*. Second ed.; Surfside Scientific Publishers: Gainesville, FL, 1992.

30. Fan, Z.; Lu, J., *Journal of nanoscience and nanotechnology* **2005,** *5*, 1561-1573.

31. Galdámez-Martinez, A.; Santana, G.; Güell, F.; Martínez-Alanis, P. R.; Dutt, A., *Nanomaterials* **2020,** *10* (5), 857.

32. Yao, Y.-F.; Chou, K.-P.; Lin, H.-H.; Chen, C.-C.; Kiang, Y.-W., *ACS Applied Materials and Interfaces* **2018,** *10*, 40764-40772.

33. Lin, H.-J.; Baltrus, J. P.; Gao, H.; Ding, Y.; Nam, C.-Y.; Ohodnicki, P.; Gao, P.-X., *ACS Applied Materials & Interfaces* **2016,** *8* (14), 8880-8887.

34. Krishna, J. V. S.; Reddy, G.; Devulapally, K.; Islavath, N.; Giribabu, L., *Optical Materials* **2019,** *95*, 109243.

35. Chen, F.-S.; Ma, J.-S.; Lu, C.-H., *Ceramics International* **2012,** *38* (6), 5319-5323.

36. Chun, H. J.; Choi, Y. S.; Bae, S. Y.; Seo, H. W.; Hong, S. J.; Park, J.; Yang, H., *The Journal of Physical Chemistry B* **2003,** *107* (34), 9042-9046.

37. ASTM E1021-15(2019), Standard Test Method for Spectral Responsivity Measurements of Photovoltaic Devices. ASTM International, West Conshohococken, PA, 2019.

38. G2V Optics, Inc., Small Area Class AAA LED Solar Simulator. https://g2voptics.com/solar-simulation/pico-solar-simulator/ (accessed June 7).

39. G2V Optics, Inc. How To Test Solar Cells. https://g2voptics.com/photovoltaics-solar-cells/solar-cell-testing/#iv-of-a-solar-cellr Cells (g2voptics.com) (accessed June 7).

40. Smestad, G. P.; Gratzel, M., *Journal of Chemical Education* **1998,** *75* (6), 752.

41. Abrams, N. Constructing a Dye Sensitized Solar Cell. https://www.youtube.com/watch?v=17SsOKEN5dE (accessed January 7).

42. Tanaka, J.; Suib, S. L., *Journal of Chemical Education* **1984,** *61* (12), 1104.

# APPENDIX

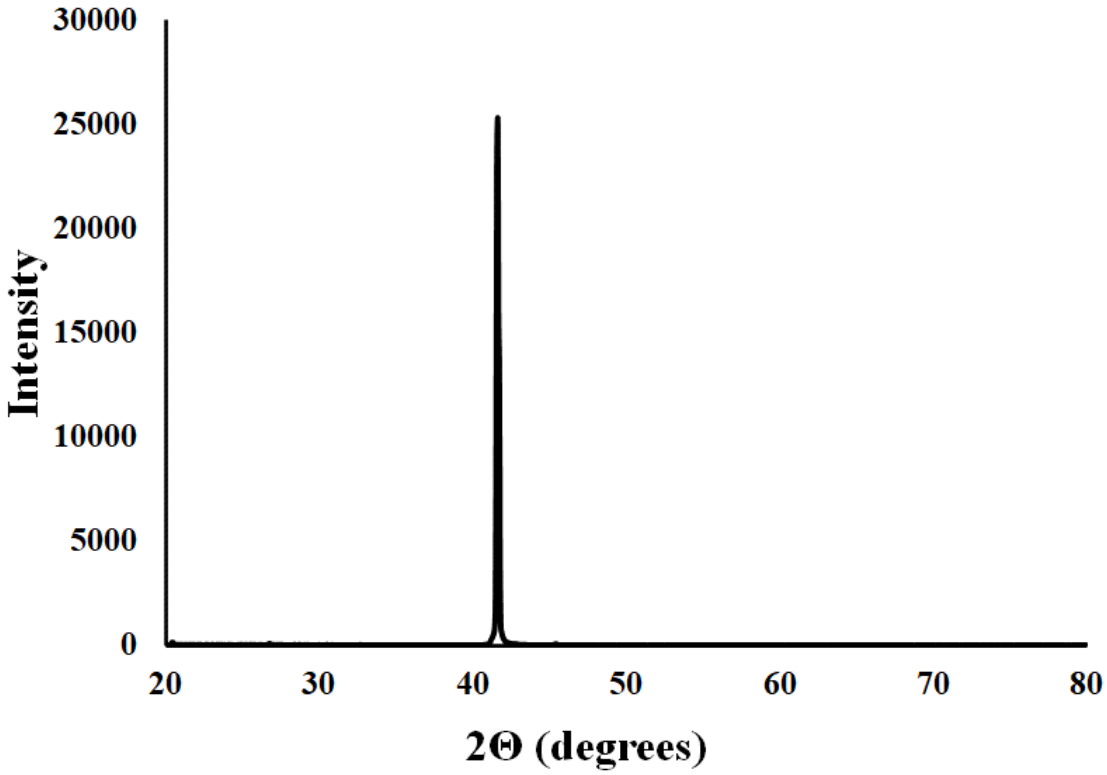


Diffractogram of a *c*-plane sapphire substrate

(Rigaku MiniFlex600 powder x-ray diffractometer)

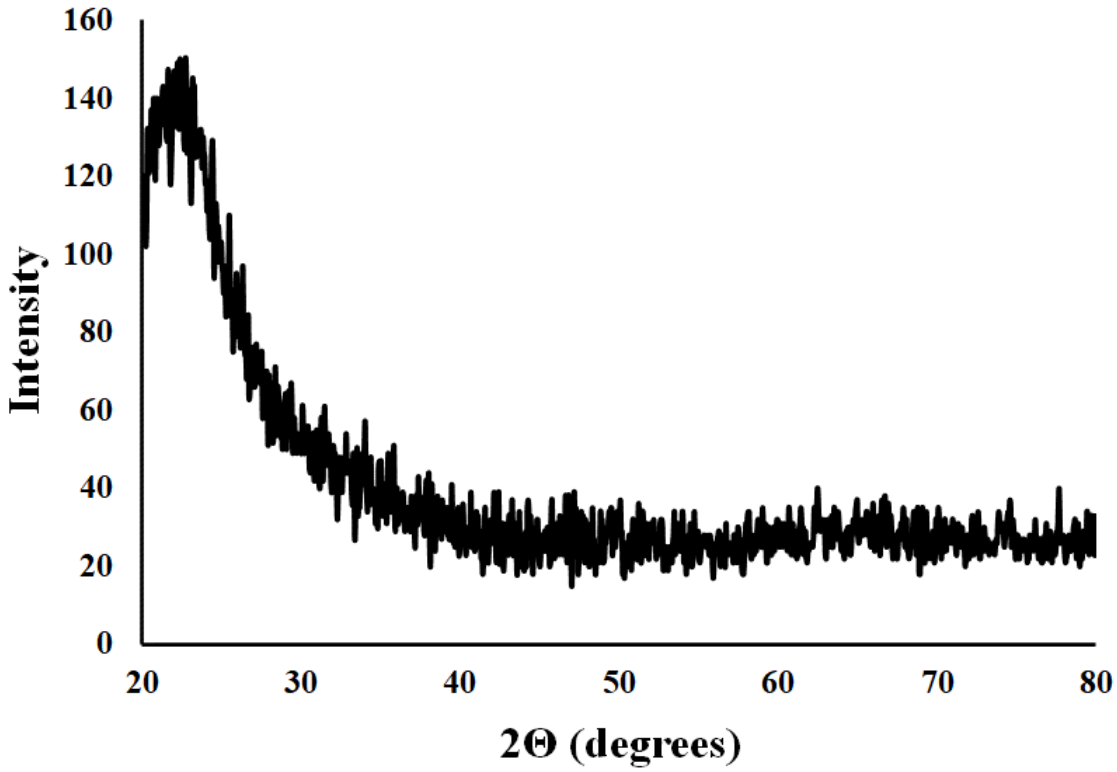


Diffractogram of a fused quartz substrate

(Rigaku MiniFlex600 powder x-ray diffractometer)

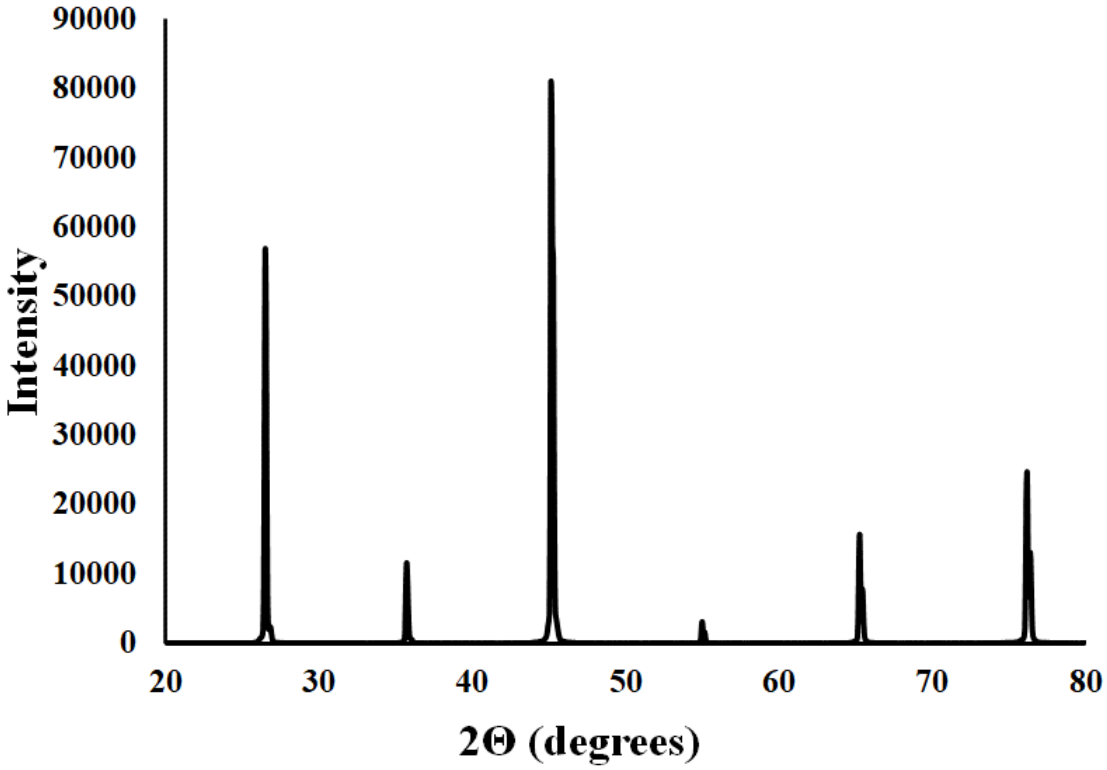


Diffractogram of a mica substrate

(Rigaku MiniFlex600 powder x-ray diffractometer)

**VITA**

# Hailey Stephen

## Education

**Master of Science in Chemistry**
Sam Houston State University, College of Science and Engineering Technology
Huntsville, TX
August 2019 – Present (expected graduation: July 2021)

**Bachelor of Science in Chemistry**
Tarleton State University, College of Science and Technology
Stephenville, TX
August 2016 – May 2019

## Skills

- Knowledgeable in analytical methods: UV-Vis, fluorescence, GC-FID, GC-MS, ICP-AES, ion chromatography, and gel electrophoresis.
- Proficient in performing statistics, dimensional analysis, and other mathematical operations.

## Experience

**Graduate Teaching Assistant**, Sam Houston State University
September 2019 – May 2021

- Taught undergraduate analytical labs, graded student work, prepared laboratory chemicals, engaged in troubleshooting minor instrument problems, and provided constructive feedback to students and instructors.
- Guided students in operating UV-Vis spectrophotometers, fluorescence spectrophotometers, flame AA, ICP-AES, GC-FID, and GC-MS.

| | |
|---|---|
| Fall 2019 | Quantitative Analysis and Instrumental Analysis |
| Spring 2020 | General Chemistry I |
| Fall 2020 | Quantitative Analysis and Instrumental Analysis |
| Spring 2021 | Quantitative Analysis |

**Graduate Chemistry Research Assistant**, Sam Houston State University
September 2019 – Present

- Synthesizing transparent conducting oxide nanostructures.
- Collecting data using powder XRD and room temperature photoluminescence.

**Undergraduate Chemistry Research Assistant**, Tarleton State University
May 2018 – May 2019

- Tested conductometric methods for detection of sulfate in swine.
- Used ion chromatography to confirm the findings of the conductometric studies.
- Presented research at chapter and national meetings.

"Measurement of Sulfate in Swine Urine by Conductometric Titration and Ion Chromatography"
Hailey Stephen, Shey Andrews, and Linda Schultz
April 1, 2019
275th ACS National Meeting, Orlando, FL.

**Chemistry Tutor**, Tarleton State University
August 2017 – May 2019

- Assisted students in learning fundamental chemistry concepts.
- Organized sessions to facilitate a learning environment.
- Documented student progress and kept records for each session.